STATE OF THE CLIMATE IN 2023

ANTARCTICA AND THE SOUTHERN OCEAN

K. R. Clem and M. N. Raphael, Eds.

Special Online Supplement to the *Bulletin of the American Meteorological Society*, Vol. 105, No. 8, August 2024

https://doi.org/10.1175/BAMS-D-24-0099.1

Corresponding author: Kyle R. Clem / kyle.clem@vuw.ac.nz

STATE OF THE CLIMATE IN 2023
Antarctica and the Southern Ocean

Editors

Jessica Blunden
Tim Boyer

Chapter Editors

Anthony Arguez
Josh Blannin
Peter Bissolli
Kyle R. Clem
Howard J. Diamond
Matthew L. Druckenmiller
Robert J. H. Dunn
Catherine Ganter
Nadine Gobron
Gregory C. Johnson
Rick Lumpkin
Rodney Martinez
Ademe Mekonnen
John B. Miller
Twila A. Moon
Marilyn N. Raphael
Carl J. Schreck III
Laura Stevens
Richard L. Thoman
Kate M. Willett
Zhiwei Zhu

Technical Editor

Lukas Noguchi

BAMS Special Editor for Climate

Timothy DelSole

American Meteorological Society

Cover Credit:
Summer ice floes in December 2015. Photo taken by Dr Sandy Thomalla on board the SA Agulhas II during the third Southern Ocean Seasonal Cycle Expedition (SOSCEx III).

How to cite this document:
Antarctica and the Southern Ocean is one chapter from the *State of the Climate in 2023* annual report and is available from https://doi.org/10.1175/BAMS-D-24-0099.1. Compiled by NOAA's National Centers for Environmental Information, *State of the Climate in 2023* is based on contributions from scientists from around the world. It provides a detailed update on global climate indicators, notable weather events, and other data collected by environmental monitoring stations and instruments located on land, water, ice, and in space. The full report is available from https://doi.org/10.1175/2024BAMSStateoftheClimate.1.

Citing the complete report:
Blunden, J. and T. Boyer, Eds., 2024: "State of the Climate in 2023". *Bull. Amer. Meteor. Soc.*, **105** (8), Si–S483 https://doi.org/10.1175/2024BAMSStateoftheClimate.1.

Citing this chapter:
Clem, K. R. and M. N. Raphael, Eds., 2024: Antarctica and the Southern Ocean [in "State of the Climate in 2023"]. *Bull. Amer. Meteor. Soc.*, **105** (8), S331–S370, https://doi.org/10.1175/BAMS-D-24-0099.1.

Citing a section (example):
Trusel, L. D., R. Baiman, C. Amory, D. Bozkurt, R. T. Datta, P. Deb, J. Kromer, and M. L. Maclennan, 2024: Ice-sheet surface mass balance [in "State of the Climate in 2023"]. *Bull. Amer. Meteor. Soc.*, **105** (8), S343–S345, https://doi.org/10.1175/BAMS-D-24-0099.1.

Editor and Author Affiliations (alphabetical by name)

Adusumilli, Susheel, Scripps Institution of Oceanography, University of California, San Diego, La Jolla, California

Amory, Charles, Université Grenoble Alpes, Institut des Géosciences de l'Environnement, IRD, CNRS, Grenoble INP, Grenoble, France

Baiman, Rebecca, Department of Atmospheric and Oceanic Sciences, University of Colorado Boulder, Boulder, Colorado

Banwell, Alison F., Earth Science and Observation Center, Cooperative Institute for Research in Environmental Sciences (ESOC/CIRES), University of Colorado Boulder, Boulder, Colorado

Barreira, Sandra, Argentine Naval Hydrographic Service, Buenos Aires, Argentina

Beadling, Rebecca L., Department of Earth and Environmental Science, Temple University, Philadelphia, Pennsylvania

Bozkurt, Deniz, Department of Meteorology, University of Valparaíso, Valparaíso, Chile; Center for Climate and Resilience Research (CR)2, Santiago, Chile

Clem, Kyle R., School of Geography, Environment and Earth Sciences, Victoria University of Wellington, Wellington, New Zealand

Colwell, Steve, British Antarctic Survey, Cambridge, United Kingdom

Coy, Lawrence, Science Systems and Applications, Inc., Lanham, Maryland; NASA Goddard Space Flight Center, Greenbelt, Maryland

Datta, Rajashree T., Department of Atmospheric and Oceanic Sciences, University of Colorado Boulder, Boulder, Colorado

Deb, Pranab, Centre for Ocean, River, Atmosphere and Land Sciences (CORAL), Indian Institute of Technology Kharagpur, Kharagpur, India

De Laat, Jos, Royal Netherlands Meteorological Institute (KNMI), DeBilt, The Netherlands

du Plessis, Marcel, Department of Marine Sciences, University of Gothenburg, Gothenburg, Sweden

Fernandez, Denise, National Institute of Water and Atmospheric Research, Ltd. (NIWA) Auckland, New Zealand

Fogt, Ryan L., Department of Geography, Ohio University, Athens, Ohio

Fricker, Helen A., Scripps Institution of Oceanography, University of California, San Diego, La Jolla, California

Gille, Sarah T., Scripps Institution of Oceanography, University of California, San Diego, La Jolla, California

Johnson, Bryan, NOAA/OAR Earth System Research Laboratory, Global Monitoring Laboratory, Boulder, Colorado; University of Colorado Boulder, Boulder, Colorado

Josey, Simon A., Marine Systems Modelling, National Oceanography Center, Southampton, United Kingdom

Keller, Linda M., Department of Atmospheric and Oceanic Sciences, University of Wisconsin-Madison, Madison, Wisconsin; Antarctic Meteorological Research and Data Center, Space Science and Engineering Center, University of Wisconsin-Madison, Madison, Wisconsin

Kramarova, Natalya A., NASA Goddard Space Flight Center, Greenbelt, Maryland

Kromer, Jessica, Department of Geography, Pennsylvania State University, State College, Pennsylvania

Lait, Leslie, R., Science Systems and Applications, Inc., Lanham, Maryland; NASA Goddard Space Flight Center, Greenbelt, Maryland

Lazzara, Matthew A., Department of Physical Sciences, School of Science, Technology, Engineering, and Mathematics, Madison Area Technical College, Madison, Wisconsin; Antarctic Meteorological Research and Data Center, Space Science and Engineering Center, University of Wisconsin-Madison, Madison, Wisconsin

Lieser, Jan L., Bureau of Meteorology, Melbourne, Australia; Institute for Marine and Antarctic Studies (IMAS), University of Tasmania, Hobart, Australia

MacFerrin, Michael, Earth Science and Observation Center, CIRES, University of Colorado, Boulder, Colorado

MacGilchrist, Graeme M., University of St. Andrews, St Andrews, United Kingdom

MacLennan, Michelle L., Department of Atmospheric and Oceanic Science, University of Colorado Boulder, Boulder, Colorado

Marouchos, Andreas, CSIRO Environment, Canberra, Australia

Massom, Robert A., Australian Antarctic Division, Australian Antarctic Program Partnership (AAPP) and Australian Centre for Excellence in Antarctic Science (ACEAS), Hobart, Australia

McMahon, Clive R., Sydney Institute of Marine Science, IMOS Animal Tagging, Mosman, Australia

Mikolajczyk, David E., Antarctic Meteorological Research and Data Center, Space Science and Engineering Center, University of Wisconsin-Madison, Madison, Wisconsin

Mote, Thomas L., Department of Geography, University of Georgia, Athens, Georgia

Newman, Paul A., NASA Goddard Space Flight Center, Greenbelt, Maryland

Norton, Taylor, Antarctic Meteorological Research and Data Center, Space Science and Engineering Center, University of Wisconsin-Madison, Madison, Wisconsin

Petropavlovskikh, Irina, NOAA/OAR Earth System Research Laboratory, Global Monitoring Laboratory, Boulder, Colorado; University of Colorado Boulder, Boulder, Colorado

Pezzi, Luciano P., National Institute for Space Research (INPE), São José dos Campos, São Paulo, Brazil

Pitts, Michael, NASA Langley Research Center, Hampton, Virginia

Raphael, Marilyn N., Department of Geography, University of California, Los Angeles, Los Angeles, California

Reid, Phillip, Bureau of Meteorology, Melbourne, Australia; Australian Antarctic Program Partnership (AAPP), Hobart, Australia

Santee, Michelle L., NASA Jet Propulsion Laboratory, Pasadena, California

Scambos, Theodore A., Cooperative Institute for Research in Environmental Sciences, University of Colorado Boulder, Boulder, Colorado

Schulz, Cristina, Department of Marine and Environmental Sciences, Northeastern University, Massachusetts

Shi, Jia-Rui, Woods Hole Oceanographic Institution, Woods Hole, Massachusetts

Souza, Everaldo, Federal University of Pará (UFPA), Belém, Brazil

Stammerjohn, Sharon, Institute of Arctic and Alpine Research, University of Colorado Boulder, Boulder, Colorado

Thomalla, Sandy, Southern Ocean Carbon-Climate Observatory, Council for Scientific and Industrial Research (CSIR), Pretoria, South Africa; Marine and Antarctic Research Centre for Innovation and Sustainability, Department of Oceanography, University of Cape Town, Cape Town, South Africa

Tripathy, Sarat Chandra, National Centre for Polar and Ocean Research, Vasco da Gama, India

Trusel, Luke D., Department of Geography, Pennsylvania State University, State College, Pennsylvania

Turner, Katherine, Department of Geosciences, University of Arizona, Tucson, Arizona; Geophysical Fluid Dynamics Laboratory, Princeton, New Jersey; Department of Atmospheric and Oceanic Sciences, Princeton University, Princeton, New Jersey

Yin, Ziqi, Department of Atmospheric and Oceanic Sciences, University of Colorado Boulder, Boulder, Colorado

Editorial and Production Team

Allen, Jessicca, Graphics Support, Cooperative Institute for Satellite Earth System Studies, North Carolina State University, Asheville, North Carolina

Camper, Amy V., Graphics Support, Innovative Consulting and Management Services, LLC, NOAA/NESDIS National Centers for Environmental Information, Asheville, North Carolina

Haley, Bridgette O., Graphics Support, NOAA/NESDIS National Centers for Environmental Information, Asheville, North Carolina

Hammer, Gregory, Content Team Lead, Communications and Outreach, NOAA/NESDIS National Centers for Environmental Information, Asheville, North Carolina

Love-Brotak, S. Elizabeth, Lead Graphics Production, NOAA/NESDIS National Centers for Environmental Information, Asheville, North Carolina

Ohlmann, Laura, Technical Editor, Innovative Consulting and Management Services, LLC, NOAA/NESDIS National Centers for Environmental Information, Asheville, North Carolina

Noguchi, Lukas, Technical Editor, Innovative Consulting and Management Services, LLC, NOAA/NESDIS National Centers for Environmental Information, Asheville, North Carolina

Riddle, Deborah B., Graphics Support, NOAA/NESDIS National Centers for Environmental Information, Asheville, North Carolina

Veasey, Sara W., Visual Communications Team Lead, Communications and Outreach, NOAA/NESDIS National Centers for Environmental Information, Asheville, North Carolina

6. Table of Contents

6. ANTARCTICA AND THE SOUTHERN OCEAN

K. R. Clem and M. N. Raphael, Eds.

a. Overview

—K. R. Clem

Antarctica experienced strong to record below-average pressure and stronger-than-average circumpolar westerlies to start (January) and close (December) 2023, marking the third and fourth consecutive summers with such conditions (2020/21, 2021/22, 2022/23, 2023/24). During austral autumn, winter, and spring, the atmospheric circulation over the South Pacific underwent a marked transition from the previous three years as the "triple dip" La Niña officially transitioned to El Niño during autumn 2023. Consistent with El Niño, positive pressure anomalies developed in the Ross and Amundsen Seas, and anomalous low pressure developed over the Antarctic Peninsula and western Weddell Sea. These two circulation anomalies produced two regions of persistent warm northerly flow and above-average atmospheric river activity: across the Weddell Sea and Dronning Maud Land (on the eastern side of the low) and in the Wilkes Land region (on the western side of the high). These two regions saw Antarctica's most pronounced climate anomalies in 2023, including well-above average temperatures and surface mass balance. These anomalies were most pronounced in the Weddell Sea region where western Dronning Maud Land, Coates Land, and the Ronne-Filchner Ice Shelf saw Antarctica's highest surface mass balance anomalies for the year, and temperatures for much of the year ranged from 2°C to 6°C above average over the Weddell Sea and along coastal Dronning Maud Land. The Antarctic Peninsula also experienced well-above-average temperatures and surface melting during the 2022/23 summer melt season, marking the fourth consecutive summer of anomalous high surface melt on the Peninsula.

Overall, net surface mass balance over the ice sheet was above average in 2023; however, surface mass balance was significantly less than the record-high values seen in 2022. With closer-to-average surface mass balance, ice discharge—mainly from the West Antarctic Ice Sheet—overwhelmed surface mass gains, and the Antarctic Ice Sheet had a net ice-sheet mass loss of 170 Gt between January and November 2023. This marks a return of Antarctica contributing to sea-level rise after the short-lived record-high mass gains seen in 2022 due to record-high snowfall.

The most significant feature of the southern polar region in 2023 was the record-low sea-ice coverage over the Southern Ocean. On 21 February, Antarctic sea-ice extent and sea-ice area both reached all-time record lows of 1.85×10^6 km^2 and 1.10×10^6 km^2, respectively, surpassing the previous record lows that were set just a year earlier in February 2022. Eight months saw new monthly-mean record lows in sea-ice extent and sea-ice area, and 76% of the days in 2023 set new daily record-low sea-ice extents. Also unprecedented were the number of daily record lows that occurred during sea-ice growth months, in contrast to previous years where the record lows predominantly occurred during the summer retreat season. For example, 6 July had a record-low daily sea-ice extent that was a remarkable 1.8×10^6 km^2 lower than the previous record low for that day. Additionally, the absence of pack ice resulted in an unprecedented 154 days of record-high coastal exposure during which there was a complete lack of a protective sea-ice "buffer".

Consistent with the low sea-ice coverage, Southern Ocean sea-surface temperatures and heat content in the upper 2000 m were both well above average in 2023, marking a continuation of the Southern Ocean warming trend observed since 2005 (Cai et al. 2023). The most pronounced positive sea-surface temperature and ocean heat content anomalies were in the South Atlantic and southwest Pacific, coinciding with the two regions of warm northerly atmospheric flow

discussed above. These regions also spatially align with some of the largest deficits in sea-ice extent observed throughout most of 2023.

Lastly, the ozone hole emerged once again in the Antarctic stratosphere during late August and September 2023. The 2023 ozone hole appeared earlier than normal and persisted longer than normal, not breaking up until 20 December, while its overall size was near average and was the 16th largest in 44 years of satellite observations. The long duration of the ozone hole can be attributed to weaker planetary-scale wave activity in late spring, which resulted in stronger-than-average circumpolar westerlies and colder-than-average temperatures in the stratosphere. Additionally, anomalously high stratospheric water vapor from the January 2022 Hunga volcano eruption entered the southern polar stratosphere in early 2023 ahead of the annual formation of the polar vortex during autumn, leading to a 25% to 50% increase in water vapor observed in the stratosphere in May and June. The anomalously high water vapor increased the temperature threshold for polar stratospheric cloud formation, and thus resulted in earlier-than-normal chlorine activation, but overall, this did not appear to significantly contribute to the 2023 Antarctic ozone hole size or duration.

The remainder of this chapter provides a detailed overview of the state of Antarctica's climate and cryosphere, the Southern Ocean, and the ozone hole in 2023. The details are split into seven sections, beginning with the atmospheric circulation and temperature and ending with the 2023 ozone hole. In most cases, 2023 anomalies and standard deviations are based on the 1991–2020 climatological average unless otherwise stated due to data availability. The period of record over which "records" are determined is also provided in each respective section. The geographical locations and place names mentioned throughout the chapter are provided in Fig. 6.1.

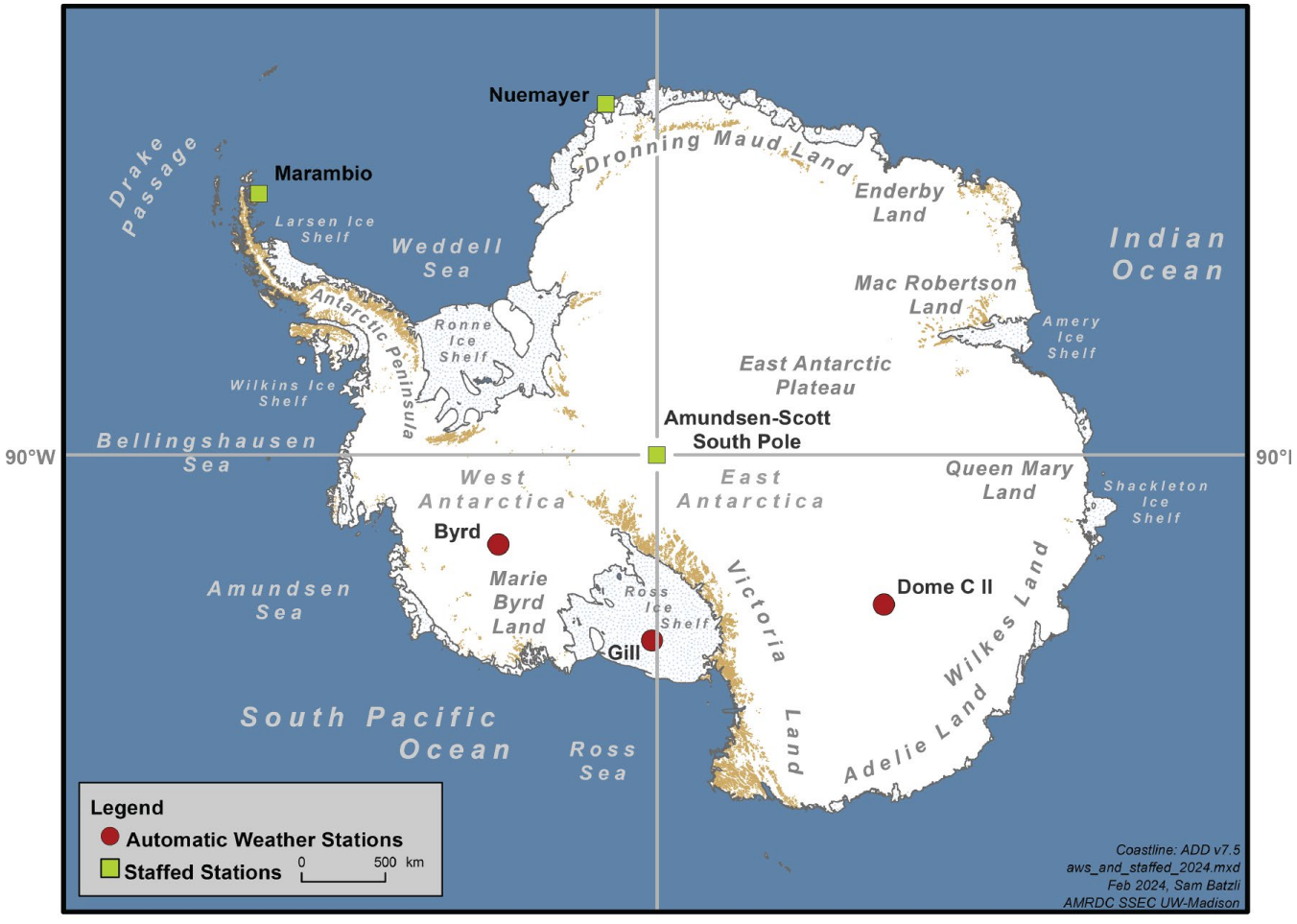

Fig. 6.1. Map of stations and geographic regions discussed in this chapter.

b. Atmospheric circulation and surface observations

—K. R. Clem, S. Barreira, S. Colwell, R. L. Fogt, L. M. Keller, M. A. Lazzara, D. E. Mikolajczyk, and T. Norton

Here we examine the major climate and atmospheric circulation anomalies across Antarctica in 2023. Monthly-mean atmospheric circulation and temperature data are from ERA5 (Hersbach et al. 2020). Figure 6.2 shows the vertical structure of the monthly geopotential height (Fig. 6.2a) and temperature (Fig. 6.2b) anomalies averaged over the polar cap (60°S–90°S) and the monthly circumpolar zonal wind anomalies (Fig. 6.2c) averaged over 50°S–70°S; the monthly Marshall (2003) Southern Annular Mode (SAM) index is provided at the bottom of Fig. 6.2. Despite masking individual months, the surface climate anomalies were grouped into and averaged across four periods of relatively persistent patterns seen in 2023: January–March, April–June, July–September, and October–December (Fig. 6.3). Observed monthly temperature and pressure anomalies for select Antarctic staffed and automatic weather stations (AWS) are also examined in Fig. 6.4; see Fig. 6.1 for station locations. The period of record for the stations is provided in the caption of Fig. 6.4.

January 2023 was marked by strong negative geopotential height (Fig. 6.2a) and surface pressure (Fig. 6.3a) anomalies across Antarctica (>2 std. dev. below average), and the circumpolar westerlies (Fig. 6.2c) were much stronger than average (+2 m s^{-1} to +5 m s^{-1}, 2–2.5 std. dev. above average). This pattern initially developed the month prior in December 2022 and thus continued into January 2023. The below-average pressure and strong circumpolar westerlies extended vertically through the depth of the troposphere and stratosphere, while at the surface almost all stations in East Antarctica set record-low monthly pressure values in January: Amundsen-Scott and Dome C II AWS (shown in Figs. 6.4c,d), as well as Relay AWS, Vostok and all coastal East Antarctic stations (not shown) had record-low pressure in January. The Marshall (2003) SAM index in January was also record high for January (+4.6) and the second highest on record for any month (both since 1957); the NOAA Climate Prediction Center's Antarctic Oscillation index (defined as the leading mode of monthly 700-hPa geopotential height anomalies) in January was also the highest January value on record (since 1979; not shown). During February and March, the polar-cap geopotential height and the

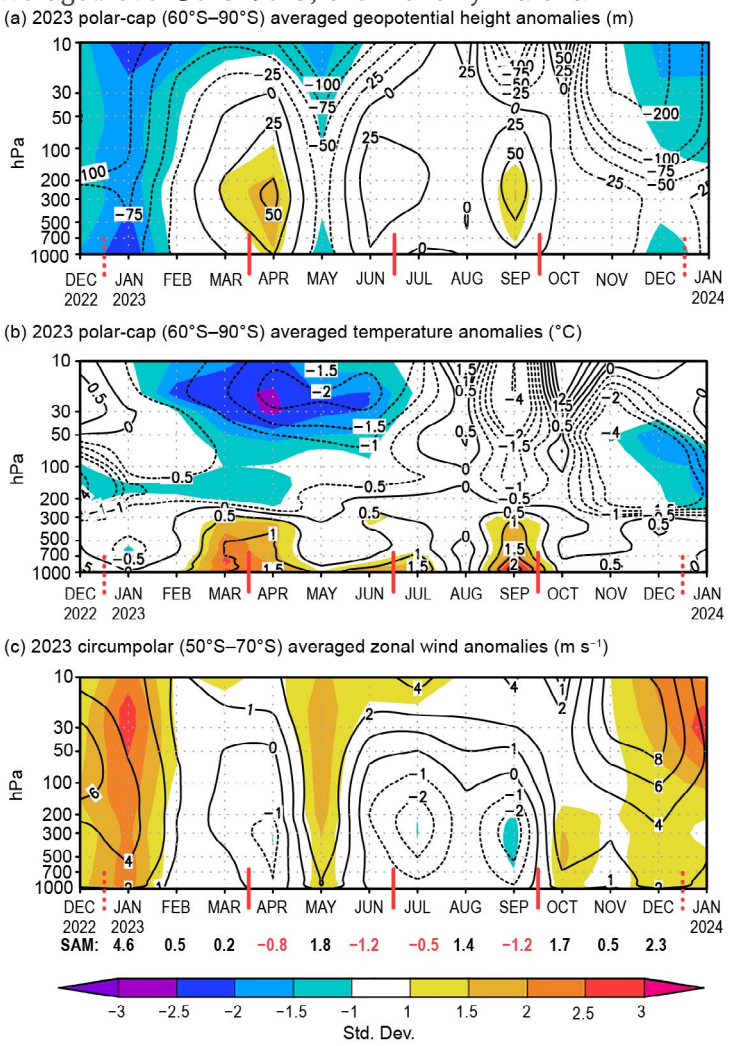

Fig. 6.2. Area-averaged (weighted by cosine of latitude) monthly anomalies over the southern polar region in 2023 relative to 1991–2020: (a) polar-cap (60°S–90°S) averaged geopotential height anomalies (m; contour interval is 25 m up to ±100 m and 100 m after ±100 m); (b) polar-cap averaged temperature anomalies (°C; contour interval is 0.5°C up to ±2°C and 2°C after ±2°C); (c) circumpolar (50°S–70°S) averaged zonal wind anomalies (m s^{-1}; contour interval is 2 m s^{-1} with an additional contour at ±1 m s^{-1}). Shading depicts standardized monthly anomalies as indicated by the color bar at the bottom. Red vertical bars indicate the four climate periods used for compositing in Fig. 6.3; the dashed lines near Dec 2022 and Dec 2023 indicate circulation anomalies wrapping around the calendar year. Values from the Marshall (2003) Southern Annular Mode (SAM) index are shown below (c) in black (positive values) and red (negative values). (Source: ERA5 reanalysis.)

circumpolar westerly wind anomalies dissipated and returned to their long-term average (Fig. 6.2).

Regionally, the January–March average surface pressure anomalies (Fig. 6.3a) reveal the strongest and most persistent negative pressure/cyclonic anomaly was located over the Bellingshausen Sea (reflecting a deep Amundsen Sea Low) where pressure was 8 hPa–10 hPa below average (>3 std. dev.). To the east of the cyclone, where warm northerly flow prevailed, Antarctic Peninsula temperatures were 1°C–3°C above average during January–March (Figs. 6.3b, 6.4ba), Antarctic Peninsula surface melt was 56% above the baseline median average in January–February (see section 6d, Fig. 6.8b), and there was an above-average number of atmospheric rivers and snowfall/surface mass balance across the Ronne-Filchner Ice Shelf in March (see section 6c, Fig. 6.6b). To the west of the cyclone, cold offshore flow resulted in substantially less-than-average surface melt across coastal West Antarctica, Wilkes Land, and Adélie Land during January–February. These regional impacts associated with the deep Amundsen Sea Low are consistent with previous studies (e.g., Raphael et al. 2016) as well as the impact of large-scale modes of variability on the depth of the Amundsen Sea Low, namely the La Niña conditions (see section 4b) and the strongly positive SAM conditions that were observed during this period (Clem and Fogt 2013; Ding and Steig 2013). Lastly, the vertical temperature profile reveals a strong positive temperature anomaly that developed over the polar cap in March (>1.0°C, 2 std. dev. averaged) despite near-average circulation (SAM index of 0.2), while this was contrasted by strong negative temperature anomalies in the stratosphere during February and March (1°C–2°C below average, >2 std. dev.).

From April to June, the monthly polar-cap averaged pressure anomalies flipped from strongly positive in April (Figs. 6.2a, 6.4)—during which Amundsen-Scott recorded its highest monthly-mean April pressure on record (Fig. 6.4c)—to negative in May, including a brief but intense strengthening of the circumpolar westerlies (Fig. 6.2c), then back to positive in June. The most

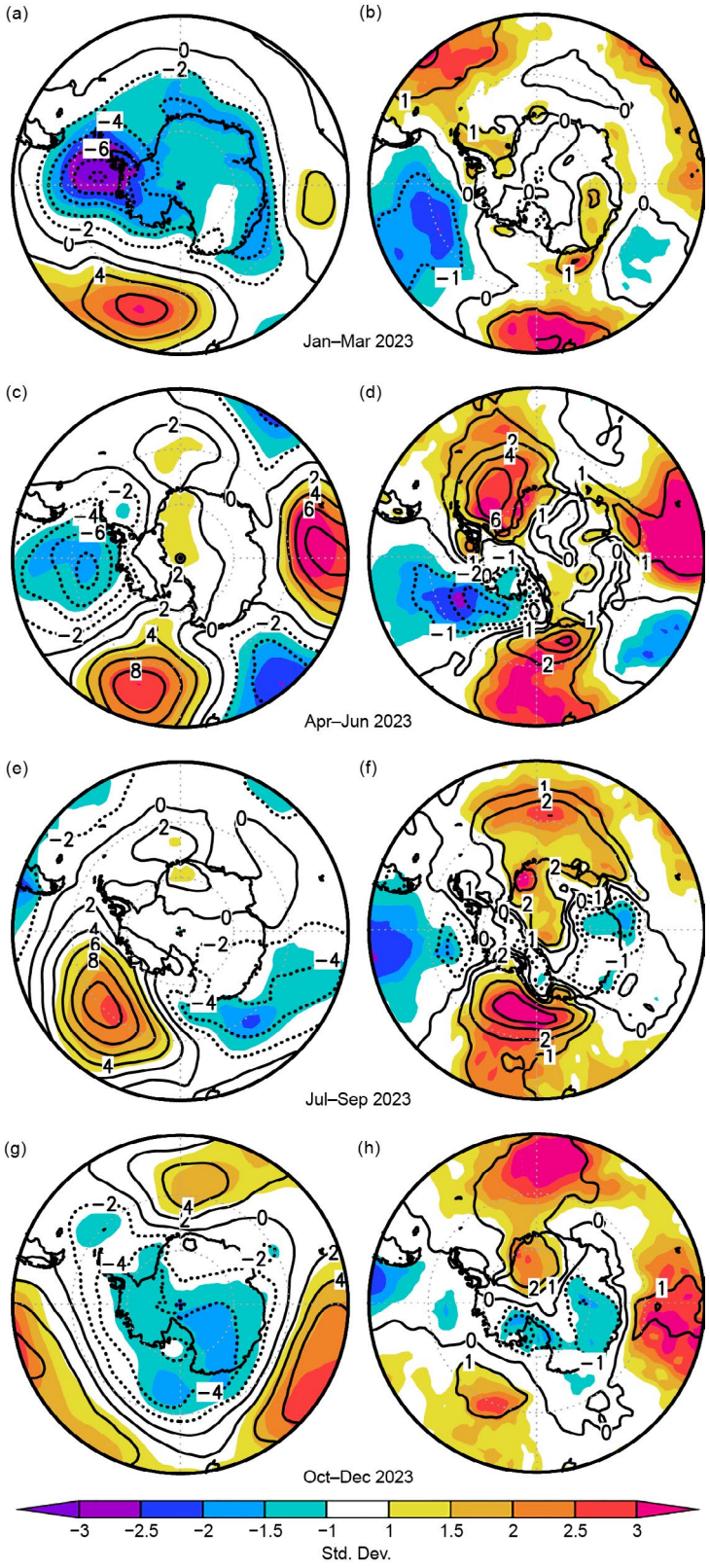

Fig. 6.3. (left) Surface pressure (hPa) and (right) 2-m temperature (°C) anomalies relative to 1991–2020 for (a),(b) Jan–Mar 2023; (c),(d) Apr–Jun 2023; (e),(f) Jul–Sep 2023, and (g),(h) Oct–Dec 2023. Contour interval is 2 hPa for surface pressure anomalies and 1°C for 2-m temperature anomalies. Shading shows the standardized anomalies. (Source: ERA5 reanalysis.)

pronounced surface pressure anomalies averaged over April–June continued to be a strong negative pressure/cyclonic anomaly in the Bellingshausen Sea, but a strong ridge of high pressure also developed over Dronning Maud Land and the adjacent South Atlantic from April onward (Fig. 6.3c; the three-month average dampens the most intense positive pressure anomaly in April). Together, this cyclone-anticyclone pair produced intense warm northerly flow across the South Atlantic sector, resulting in positive temperature anomalies of +4°C to +6°C (2–3 std. dev.) across the Weddell Sea averaged over April–June as well as a substantial delay (by up to 60 days) in sea-ice advance across the South Atlantic/Weddell Sea (see section 6f, Fig. 6.12a). In coastal Dronning Maud Land, Neumayer recorded its warmest April on record (–11.2°C, 7.0°C above average) when the ridge of high pressure over the South Atlantic and Dronning Maud Land was strongest (Fig. 6.4b).

The anomalously deep Amundsen Sea Low that dominated late summer and autumn was consistent with the (weakening) La Niña conditions in the tropical Pacific (Ding and Steig 2013). During the winter months (July–September), La Niña transitioned to El Niño (see section 4b) and the deep Amundsen Sea Low dissipated while a pronounced positive pressure anomaly developed off the coast of West Antarctica (Fig. 6.3e). With the anomalous anticyclonic/counterclockwise circulation centered north of the Ross and Amundsen Seas, cold offshore flow developed over Marie Byrd Land (Fig. 6.3f), which was most marked in August when Byrd AWS recorded its coldest August on record (–45.6°C, 10.7°C below average; Fig. 6.4e). The anticyclone shifted eastward to the Bellingshausen Sea in September (not shown, but seen in the pressure anomalies at Marambio in Fig. 6.4a). This resulted in warm northerly flow to the Ross Ice Shelf in September where Gill AWS had its warmest September on record (–26.3°C, 11.4°C above average; Fig. 6.4f). Meanwhile, the strong positive pressure anomalies across coastal Dronning Maud Land and the South Atlantic continued, producing locally intense anomalous warm conditions in eastern Dronning Maud Land during July–September. This region also experienced anomalous high surface mass balance through the winter (section 6c), indicating the northerly flow was both warm and moisture-rich.

During October–December, for the fourth spring/summer in a row (2020, 2021, 2022, and 2023), strong negative geopotential height and temperature anomalies and stronger-than-average circumpolar westerlies developed in the stratosphere (Fig. 6.2) in conjunction with the development of the 2023 ozone hole (see section 6h). The stronger-than-average polar vortex was associated with weaker wave activity in the stratosphere, and this helped maintain a longer-than-average ozone hole duration also like that seen in the previous three years (see section 6h). In December, the negative geopotential height and strong circumpolar westerly anomalies developed downward from the stratosphere through

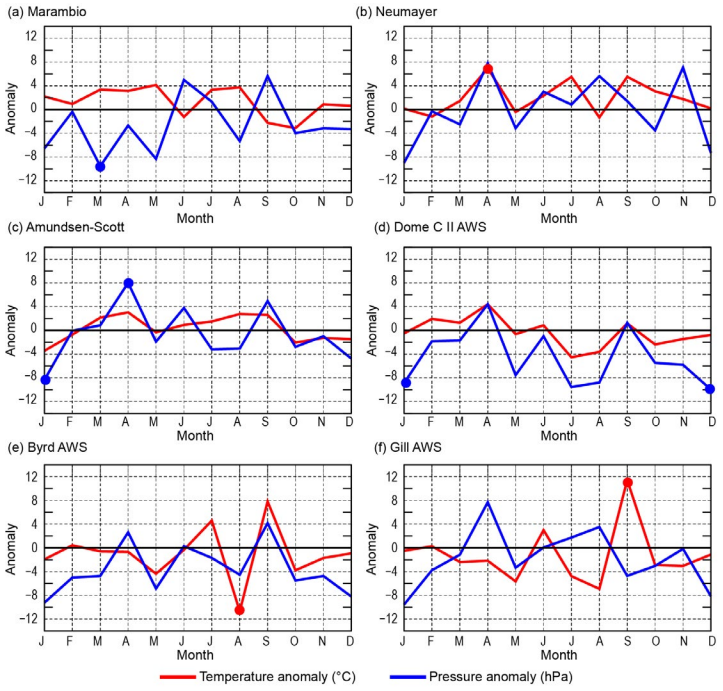

Fig. 6.4. Observed monthly Antarctic surface air temperature and station pressure anomalies during 2023 from six representative stations (three staffed [a]–[c], and three automatic [d]–[f]). Anomalies for temperature (°C) are shown in red and for mean sea-level pressure /surface pressure (hPa) are shown in blue, with filled circles denoting monthly records set for each station in 2023. All anomalies are based on the monthly 1991–2020 averages where possible. The station observation records start in 1970 for Marambio, 1981 for Neumayer, 1957 for Amundsen-Scott, 1980 for Dome C II automatic weather station (AWS), 1980 for Byrd AWS, and 1985 for Gill AWS. See Fig. 6.1 for station locations.

the troposphere, suggesting dynamical coupling between the stratosphere and troposphere circulations (Thompson et al. 2006). Strong negative pressure anomalies developed at the surface during October–December (Fig. 6.3g), also similar to the previous three years, becoming most pronounced in December when all six stations analyzed here reported below-average pressure (Fig. 6.4), and Dome C II AWS recorded its lowest monthly-mean December pressure on record.

In Dronning Maud Land, the ridge of high pressure continued and even strengthened offshore over the South Atlantic during September–December (Fig. 6.3g). This resulted in continued warm northerly flow in the South Atlantic sector and strong positive temperature anomalies of +1°C to +2°C (>2 std. dev.) in eastern Dronning Maud Land. The blocking high in the South Atlantic was strongest in November and was further coupled with a cyclonic anomaly to the west over the southeast Pacific (not shown). This coincided with an above-average number of atmospheric rivers and above-average to record-high surface mass balance across Dronning Maud Land, Coates Land, and the Ronne-Filchner ice shelf in November. Furthermore, the persistent ridge of high pressure and warm northerly flow throughout the year resulted in Neumayer recording a record-high annual average temperature of –14.0°C (2.0°C above average) in 2023.

c. Ice-sheet surface mass balance

—L. D. Trusel, R. Baiman, C. Amory, D. Bozkurt, R. T. Datta, P. Deb, J. Kromer, and M. L. Maclennan

Surface mass balance (SMB) represents the net effect of all processes that add or remove mass from the surface of an ice sheet. For the Antarctic Ice Sheet (AIS), snowfall is the dominant SMB term, with approximately 2300 Gt accumulating each year (van Wessem et al. 2018; Agosta et al. 2019; Mottram et al. 2021). Strong coast-to-plateau SMB gradients exist across the AIS (Fig. 6.5a), with typical mass gains along the coasts exceeding 500 mm water equivalent (w.e.) yr^{-1}, particularly in higher relief areas abutting the prevailing winds. In contrast, low-magnitude mass gains of <50 mm w.e. yr^{-1} are typically spread across the high-elevation plateau of the East Antarctic Ice Sheet. Much of the annual SMB gains occur during high-magnitude, extreme precipitation events, often delivered by atmospheric rivers (ARs; Turner et al. 2019; Wille et al. 2021; Maclennan et al. 2022). Sea ice can also play an influential role in SMB and precipitation patterns by modulating the amount and extent of moisture transport over the ice sheet (Kromer and Trusel 2023; Hanna et al. 2024). Snowfall-driven mass gains are countered by losses from sublimation, the leading negative SMB term for the AIS (Mottram et al. 2021). Surface melting primarily occurs across AIS ice shelves (Arthur et al. 2022; Banwell et al. 2023), with runoff and lake drainages occurring in some areas (Bell et al. 2018; Trusel et al. 2022). However, most AIS surface melt is thought to refreeze within the firn (Mottram et al. 2021), the layer of partially compacted snow from previous years located beneath the new surface snow accumulation (The Firn Symposium team 2024).

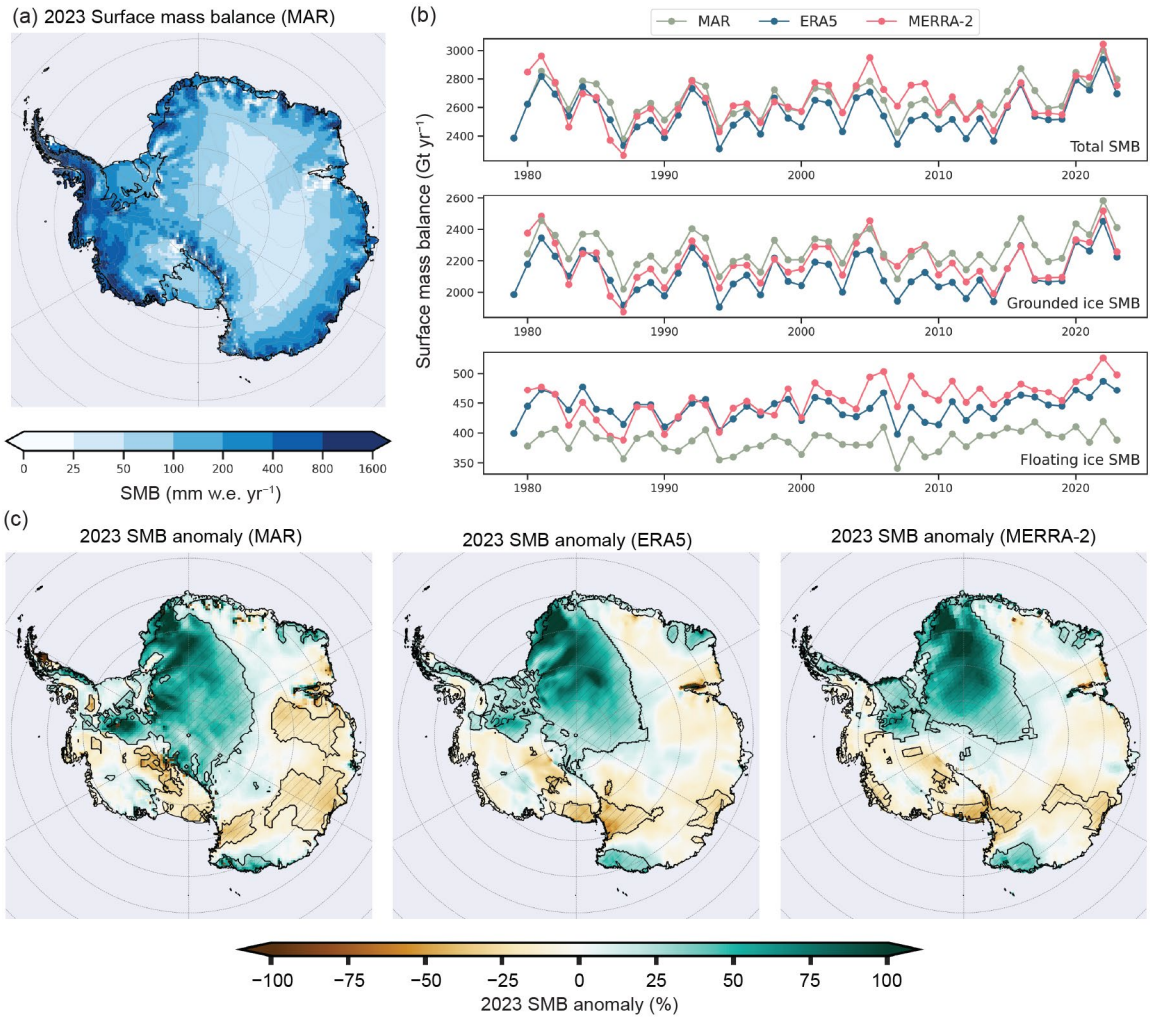

Fig. 6.5. (a) MAR 2023 surface mass balance (SMB; mm water equivalent yr^{-1}). (b) Time series of annual surface mass balance in Gt (10^{12} kg) yr^{-1} over the full ice sheet and its grounded and floating portions. (c) Annual MAR, ERA5, and MERRA-2 SMB anomalies for 2023 relative to their 1991–2020 mean (%). The 2023 SMB anomalies are higher than the 1991–2020 standard deviation of the respective datasets in the stippled areas.

Here, we use the ERA5 (Hersbach et al. 2020) and MERRA-2 (Gelaro et al. 2017) reanalyses to estimate the 2023 SMB as total precipitation minus evaporation and sublimation ($P-E$), following recent studies (e.g., Medley and Thomas 2019; Lenaerts et al. 2019). Although important biases remain associated with, for example, ice-sheet–cloud–radiation feedbacks and precipitation, evaluations of various reanalysis products over Antarctica indicate that MERRA-2 and ERA5 represent recent Antarctic climate well (Gossart et al. 2019; Medley and Thomas 2019; Wang et al. 2016). We also assess SMB as simulated by the polar-oriented regional climate model, Modèle Atmosphérique Régional (MAR), forced by ERA5 (Kittel et al. 2021). Relative to the reanalyses, MAR provides a more explicit treatment of ice-sheet surface climate and SMB, including firn evolution and meltwater runoff. Of these datasets, ERA5 is the highest resolution at 0.25°, followed by MAR at 35 km and MERRA-2 at 0.625° × 0.5°. To calculate SMB across a consistent spatial extent, we first bilinearly regridded each dataset to the ERA5 grid, following a recent SMB intercomparison (Mottram et al. 2021), before masking each using grounded and floating ice extents as defined in the Antarctic Digital Database (version 7.8; Gerrish et al. 2023). For the SMB datasets, annual and monthly anomalies are compared to 1991–2020 climatologies. We also use monthly sea-ice concentration observational data (DiGirolamo et al. 2022) and an atmospheric river (AR) detection algorithm adopted from Wille et al. (2021) applied to MERRA-2 reanalysis with a meridional moisture transport climatology of 1991–2020.

We assess SMB across both grounded and floating ice (Figs. 6.5b,c). While only the grounded SMB is relevant to sea level, SMB across floating ice shelves is important to the health of the firn layer and ice shelf stability (The Firn Symposium team 2024). The total grounded AIS SMB in 2023 equaled 2225 Gt, 2257 Gt, or 2411 Gt, according to ERA5, MERRA-2, and MAR, respectively, representing anomalies of roughly 1 std. dev. above the 1991–2020 climatological SMBs (ERA5: 2104±109 Gt yr^{-1}; MERRA-2: 2186±106 Gt yr^{-1}; MAR: 2258±97 Gt yr^{-1}). The 2023 grounded AIS SMB ranked as 11th highest since 1979 according to ERA5 (5th in MAR and 15th in MERRA-2 since 1980). Notably, 2023's grounded SMB equates to ~170 Gt, 225 Gt lower than occurred in 2022, when the AIS set a record-high SMB for the observational era in response to high snow accumulation (Datta et al. 2023), resulting in the AIS having a net positive ice-sheet mass balance in 2022 (Adusumilli et al. 2023). Thus, 2023 marked the return of a negative ice-sheet mass balance and the AIS contributing to sea-level rise driven by solid ice discharge (see section 6e for more details). Considering SMB across Antarctica's floating ice shelves only, 2023 ranked as the third and fifth highest on record in MERRA-2 and ERA5, respectively. Comparatively, ice shelf SMB is lower in MAR, both in 2023 and overall, at least partially resulting from MAR simulating surface meltwater runoff on some ice shelves. This discrepancy points to the need for improved observations and understanding of the drivers of surface melt and its magnitude. Despite elevated SMB in recent years, no method shows a significant trend for total or grounded SMB, and only MERRA-2 indicates a significant positive SMB trend for floating ice shelves (1.4 Gt yr^{-1}; $p<0.01$).

The 2023 AIS total SMB (grounded + floating) varies seasonally (Fig. 6.6a), with a minimum in austral summer (December–February; 160 Gt $month^{-1}$ to 210 Gt $month^{-1}$ in MERRA-2) and a maximum in austral autumn (March–May; 235 Gt $month^{-1}$ to 322 Gt $month^{-1}$ in MERRA-2; Fig 6.6a). Spatially, the highest SMB anomaly in 2023 was concentrated in the South Atlantic sector between 75°W and 45°E, including western Dronning Maud Land, Coates Land, and the Ronne-Filchner ice shelf (Fig. 6.5c). April, May, June, August, September, October, and November all featured anomalously high AR frequency over this region tied to the anticyclonic circulation anomalies east of AR landfall (see Figs. 6.3c,e,g). In November, this pattern resulted in a SMB anomaly of 1.5 std. dev. above the MERRA-2 climatology (Fig. 6.6a), coincident with record-high monthly-mean mean sea-level pressure values over the eastern Weddell Sea in November (since 1979, based on ERA5 reanalysis; not shown). In addition to the blocking high located off the coast of eastern Dronning Maud Land in November, a deep and elongated trough and associated surface cyclonic anomaly together produced a particularly conducive environment for AR landfall (Pohl et al. 2021; Baiman et al. 2023). The attendant cyclone had asymmetries with

shortwave troughs and ridges favorable for AR family events (Maclennan et al. 2023). Starting on 5 November, consecutive ARs made landfall just east of the Ronne-Filchner Ice Shelf over Dronning Maud Land (Fig. 6.6e) with 70% of the timesteps from 14 to 18 November featuring ARs over the AIS between 35°W and 10°W (not shown).

March was also particularly notable with total SMB anomalies exceeding 2 std. dev. in each dataset (Fig. 6.6a) and ranking as the first-, second-, or third-highest March SMB on record in MAR, MERRA-2, and ERA5, respectively. Significant and anomalous SMB in March occurred over four main regions: the Ronne-Filchner Ice Shelf, Enderby Land, Wilkes Land, and just east and west of Ross Ice Shelf (Fig. 6.6b). While AR activity near the Ronne-Filchner Ice Shelf was not anomalous in March, negative pressure anomalies (e.g., Fig. 6.3a), relatively high sea-surface temperatures (see Figs. 6.13a,b), and negative sea-ice concentration anomalies (Fig. 6.6b) likely contributed to local moisture transport and resulting snowfall. Enderby Land and Wilkes Land both saw above-average AR activity (Fig. 6.6d), consistent with high SMB anomalies. The dominant atmospheric pattern in March of higher-than-average values of surface pressure over the Ross-Amundsen Sea sector (see Fig. 6.3a), which, in combination with below-average sea ice east and west of the Ross Ice Shelf (Fig. 6.6b), is consistent with higher SMBs in these areas, particularly along the steep slopes of the Executive Committee Range.

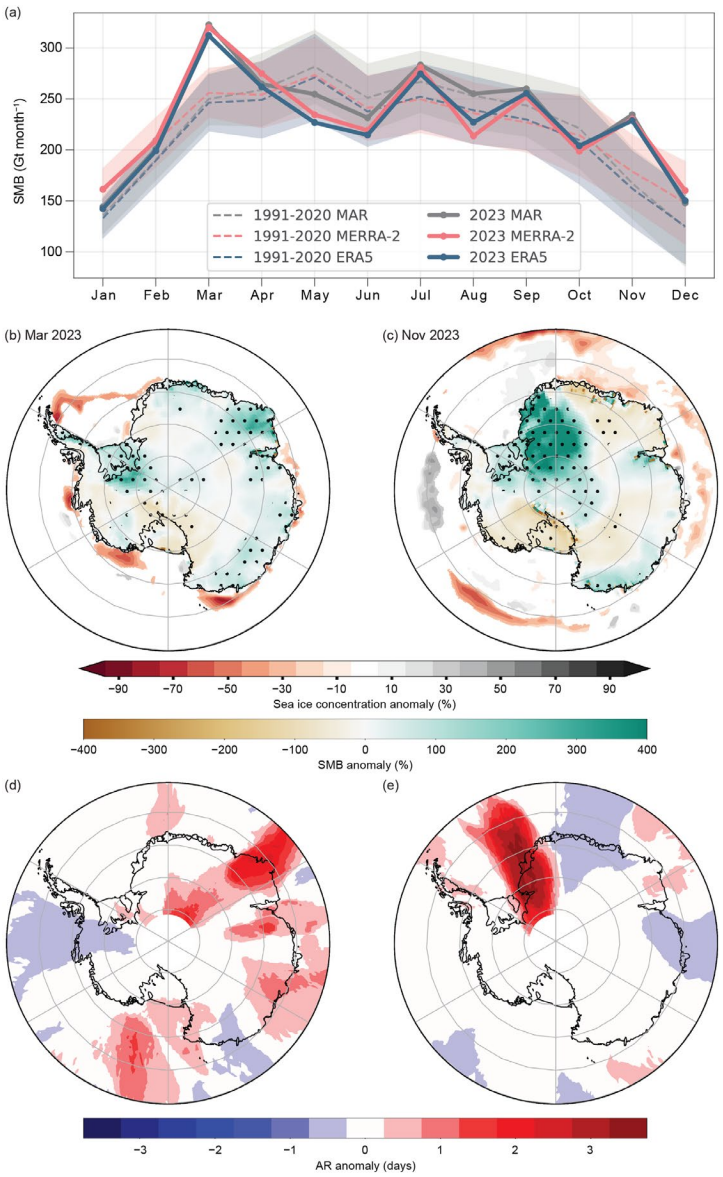

Fig. 6.6. (a) Monthly cycle of (grounded and floating) Antarctic Ice Sheet surface mass balance (SMB) in Gt month^{-1} for MERRA-2 (pink), ERA5 (blue), and MAR (gray). 2023 values are shown with a solid line, 1991–2020 average in a dotted line, 1 std. dev. is shaded. Green and brown shading over the continent shows 2023 SMB anomaly (%) for (b) Mar and (c) Nov. The 2023 SMB anomalies are higher than the 1991–2020 std. dev. of the respective datasets in the stippled areas. Stippling shows where the 2023 SMB anomalies are above or below the 1991–2020 std. dev. of the respective datasets. Gray and red shading in the Southern Ocean shows significant (>1 std. dev.) anomalous observational sea-ice concentration (%) for (b) Mar and (c) Nov. Anomalies of atmospheric river (AR) frequency (days) in (d) Mar and (e) Nov 2023 compared to 1991–2020 climatology are shown in red and blue shading.

d. Ice-sheet seasonal melt extent and duration

—M. MacFerrin, T. Mote, A. F. Banwell, Z. Yin, and T. A. Scambos

Surface melt on the Antarctic Ice Sheet (AIS) occurs primarily on the low-elevation coastal margins, especially on the Antarctic Peninsula and on the ice shelves surrounding the continent. It plays a small role in the total mass balance of the AIS relative to far larger contributions from snow accumulation, glacier calving, and basal melting. However, surface melting is a key measure of ice-sheet stability. As meltwater percolates and re-freezes, it increases the density of the underlying firn, and if melt volume is sufficient, the accumulated meltwater can induce ice-shelf break up (Banwell et al. 2013) and glacier acceleration through hydrofracture (Scambos et al. 2014).

Here, daily surface melt is mapped using satellite-derived passive-microwave brightness temperatures. The source data are distributed as daily composited polar stereographic brightness-temperatures by the National Snow and Ice Data Center (products NSIDC-0001; Meier et al. 2019 and NSIDC-0007; Gloerson 2006) spanning 1979 through the present day. Daily passive microwave brightness temperatures using the 37-GHz horizontal polarization as well as the 37- and 19-GHz vertical polarization channels are acquired by the Scanning Multichannel Microwave Radiometer (SMMR), Special Sensor Microwave/Imager (SSM/I), and Special Sensor Microwave Imager/Sounder (SSMIS) sensors aboard the NOAA Nimbus-7 and Defense Meteorological Satellite Program (DMSP) F8, F11, F13, F17, and F18 satellites. The austral melt season is defined here as 1 October through 30 April. Although small brief melt events can be measured along Antarctica's northern coastal margins during the austral winter, the vast majority of melt happens during these seven months, with the most typically occurring in December and January. An ice-extent mask of 25-km grid cells for the AIS was developed from the Quantarctica v3.0 Detailed Basemap dataset (Matsuoka et al. 2018). All 25-km cells that contain ≥50% land ice or ice shelf are included. We divide the AIS into seven melt extent and climate regions (Fig. 6.8a) by clustering glaciological drainage basins from Shepherd et al. (2012). Melt is determined by 37-GHz horizontally polarized brightness temperatures that exceed a dynamically established threshold each season from a simple microwave emission model that would be expected in the presence of liquid water in near-surface layers of ice and snowpack. The method used here was first developed to track the Greenland Ice Sheet's surface melt daily (Mote and Anderson 1995; Mote 2007, 2014). Large seasonal fluctuations in passive microwave emissions from some areas of dry polar firn in Antarctica can create false positive melt indications in an unmodified version of the Greenland algorithm. This was mitigated by filtering areas that only marginally exceed the melt threshold (<10K) in the 37-GHz horizontal polarization in regions with a negative 18/19-GHz minus 37-GHz frequency gradient in the vertical polarization and has been used in previous season reports of Antarctic melt (MacFerrin et al. 2021, 2022, 2023). We focus here on the melt season spanning 1 October 2022 through 30 April 2023. The 2023/24 Antarctic melt season will be discussed in next year's report.

According to passive-microwave satellite observations (Fig. 6.7), the 2022/23 melt season recorded an overall slightly-above-average cumulative melt index (days · area) of 7.66 million km^2 days, about 1.3% greater than the median melt index of 7.55 million km^2 days during the 1990–2020 baseline period. However, the 2022/23 melt season was punctuated by substantial spatial and temporal anomalies in individual regions. The Antarctic Peninsula (Fig. 6.8a) saw an annual melt index nearly 56% above the baseline median value (Fig. 6.8b). Antarctic Peninsula melt was affected by extensive melt events in December 2022, extended melt through the majority of January 2023, and strong melt again in early February 2023. A majority of the Larsen C, George VI, and Wilkins Ice Shelves on the Peninsula observed between 20 and 30 more melt days compared to the 1990–2020 reference period. The persistent melting was likely tied to the stronger-than-average westerly winds, a pattern reflected in the exceptionally high Marshall (2003) Southern Annular Mode (SAM) index values for November and December 2022 and January 2023 (+3.7, +2.9, and +4.6, respectively; see Fig. 6.2; Clem et al. 2023). Notably, the 2022/23 melt season marks the fourth consecutive year in which the Antarctica Peninsula had a melt index that was more than 30% higher than that of the median extent from the reference period. These four summer seasons comprise the February 2020 and February 2022 extreme

warm events on the Antarctic Peninsula tied to tropical variability (Clem et al. 2022 and Gorodetskaya et al. 2023, respectively) along with the three consecutive summers (2020/21, 2021/2022, 2022/23) of stronger-than-average circumpolar westerlies (see section 6b).

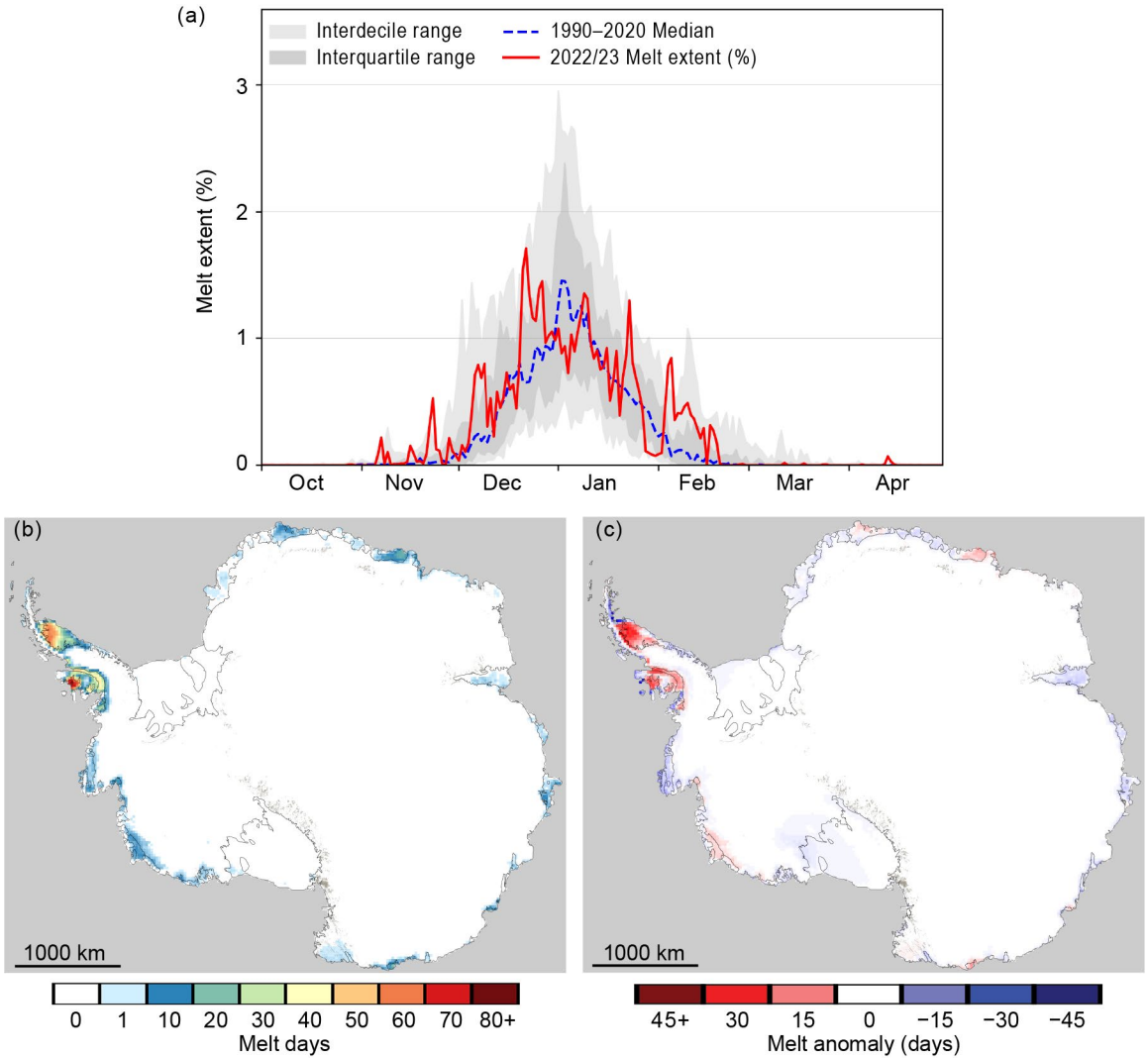

Fig. 6.7. (a) Daily surface melt extent (%) across the Antarctic Ice Sheet for the 2022/23 melt season, with 1990–2020 median values in blue and interdecile and interquartile ranges shaded in gray. (b) Map of the sum of melt days across the Antarctic Ice Sheet. (c) Map of the anomaly of the sum of melt days compared to mean values from the 1990–2020 reference period.

The Dronning Maud Land and Enderby Land (near 50°E) regions also displayed a higher-than-average-extent melt season, recording a total melt index of 41% more than the baseline period, with five extensive melt events hitting the region from late December 2022 through most of January 2023 (Fig. 6.8c). The former coincides with a region of warm northerly flow on the eastern side of a strong cyclonic anomaly over the Bellingshausen Sea and Antarctic Peninsula during January and February, while the latter coincides with warm northerly flow on the western side of an anticyclonic anomaly over the Indian Ocean (see Fig. 6.3a). Following the warmer months that are conducive for surface melt (January and February), these regions then experienced above-average surface mass balance in March (see Fig. 6.6b), suggesting regions of high surface melt transitioned to high snowfall accumulation with the onset of colder conditions. However, the Dronning Maud and Enderby Land's 2022/23 melt seasons were overall considerably less extensive than the 2021/22 melt season in which the total extent was more than triple the baseline median, as discussed in last year's report (MacFerrin et al. 2023). All other regions of the AIS observed below-average melt indices for the 2022/23 season, with the Ronne

Embayment receiving almost no observed surface melt and the Wilkes and Adélie lands region totaling only 39% melt index compared to the baseline median. Notably, the Amundsen-Bellingshausen region had a lower melt extent than average for the majority of the 2022/23 season where cold offshore flow occurred on the western side of the cyclone in the Bellingshausen Sea (see Fig. 6.3a), with the exception of an extensive event that resulted in surface melting across a majority of the Getz Ice Shelf for nearly two weeks in mid-December 2022 (Fig. 6.8d).

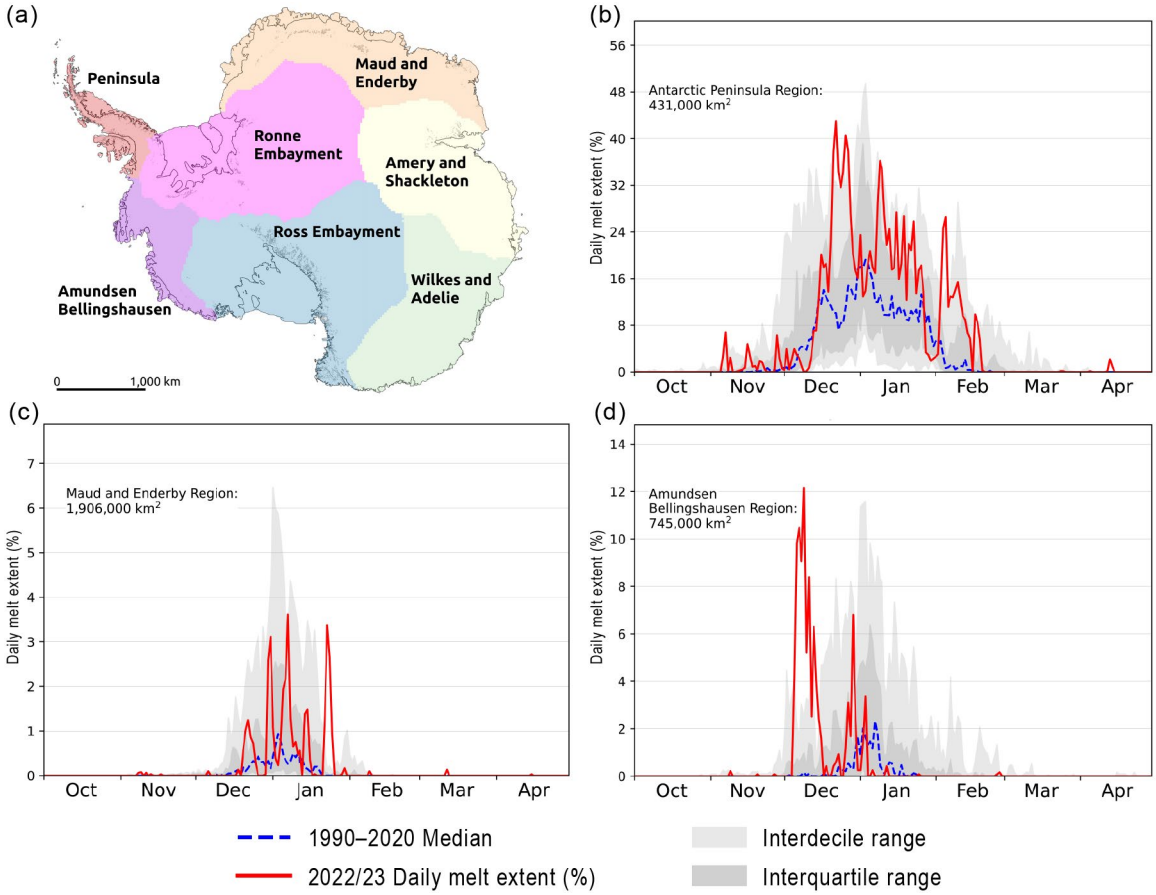

Fig. 6.8. (a) Map of Antarctic regions used in this analysis. (b)–(d) Daily 2022/23 melt extent (%) over the (b) Antarctic Peninsula region, (c) Maud and Enderby region, and (d) Amundsen Bellingshausen region.

e. Ice-sheet mass balance

—S. Adusumilli and H. A. Fricker

The mass balance of the Antarctic Ice Sheet (AIS) is the difference between mass gained through accumulation (snowfall minus sublimation) at the surface and mass lost around margins where ice is fed to the ocean through its floating ice-shelf extensions. Net ice-shelf mass loss does not add to sea level, but ice shelves play an important role in regulating the flow of grounded ice to the ocean across the grounding line through a process called "buttressing" (e.g., Gudmundsson et al. 2019). Buttressing can be reduced by an ice shelf losing mass (Paolo et al. 2015; Smith et al. 2020) or retreating from pinning points (Miles and Bingham 2024). Buttressing is lost completely if the ice shelf collapses, usually through hydrofracture (Scambos et al. 2004). Reduced buttressing leads to increased flow of ice across the grounding line, which adds to sea level (360 Gt of ice is around 1 mm global sea-level equivalent). For any given time period, the net mass balance for the grounded AIS is the difference between competing processes (mass gain from accumulation and mass loss from dynamic thinning), which depends on the integrated effects of interactions between the ice, ocean, and atmosphere (e.g., Smith et al. 2020).

Mass loss from ice shelves occurs through two main processes: calving of icebergs at ice-shelf fronts, which occurs episodically on multi-annual to multi-decadal time scales, and ocean-driven basal melting (Rignot et al. 2013; Depoorter et al. 2013; Adusumilli et al. 2020), which occurs continuously. Since 1992, the AIS has experienced overall net mass loss of grounded ice (Otosaka et al. 2023), dominated by trends in the West Antarctic Ice Sheet (WAIS). Most of this loss is attributed to net ice-shelf mass loss (Paolo et al. 2015) and a corresponding reduction in buttressing (Gudmundsson et al. 2019). Mass gains occur mainly in the interior grounded ice through changes in precipitation; as discussed in last year's report (Clem and Raphael 2023), in 2022, AIS showed record mass gains, primarily due to an increase in precipitation events over East Antarctica associated with an above-average number of landfalling atmospheric rivers.

At the time of writing, there were no published estimates of total AIS mass or height change for 2023. Here, we derived estimates of height changes over the grounded ice sheet from NASA's Ice, Cloud, and land Elevation Satellite (ICESat)-2 laser altimeter using data for 2023 until the latest available date (26 October 2023). We used the Advanced Topographic Laser Altimeter System (ATLAS)/ICESat-2 L3B Slope-Corrected Land Ice Height Time Series version 5 (Smith et al. 2022), which provides precise estimates of height along repeated ground tracks at 60-m along-track resolution. We derived along-track height changes between the available data in Cycle 21 (September/October 2023) and the corresponding data from Cycle 17 (September/October 2022; Fig. 6.9). To analyze seasonal variability, we also derived height changes over three-month intervals between successive ICESat-2 data acquisition cycles during the October 2022 to October 2023 period (Fig. 6.10). We smoothed the final height change map using a Gaussian filter with a 30-km diameter.

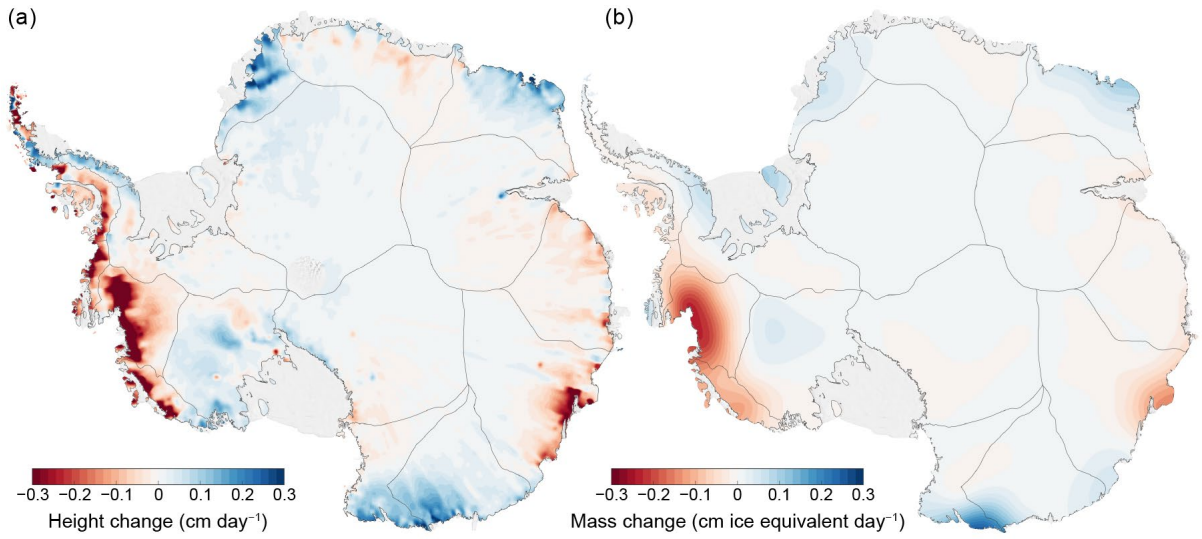

Fig. 6.9. Maps of (a) height change (cm day^{-1}) from ICESat-2 for the Oct 2022 to Oct 2023 period and (b) ice-equivalent mass change (cm ice equivalent day^{-1}) from GRACE-FO for the Oct 2022 to Oct 2023 period.

For further context, we provide annual mass anomalies derived from NASA's satellite gravimeter Gravity Recovery and Climate Experiment Follow-On (GRACE-FO; Fig. 6.9b) for 2023. We used data from the Jet Propulsion Laboratory GRACE and GRACE-FO Ocean, Ice, and Hydrology Equivalent Water Height Coastal Resolution Improvement (CRI) Filtered Release 06 version 02 "mascon data". Mascons (or mass concentration blocks) are 3° × 3° spherical caps placed on an elliptical approximation of Earth's surface over which these data are provided (Wiese et al. 2023a). We calculated gravity-derived mass anomalies for approximately the same period as used for ICESat-2 (November 2022 to November 2023), with the same three-month averaging. To determine ice-sheet mass anomalies, we identified all mascons containing more than 10,000 km^2 of land, according to the provided CRI land mask. We interpolated the area-averaged rates of change using bilinear interpolation according to the location of the geometric center of the land area contained within the mascon. We then masked all non-land areas using the Bedmachine ice mask (Morlighem et al. 2020). We also retrieved time series of mass changes integrated over the ice sheet (Fig. 6.10a) from the Level 4 Antarctica Mass Anomaly Time Series data product (Wiese et al. 2023b).

The maps of annual changes in ice-sheet height from ICESat-2 (Fig. 6.9a) and mass from GRACE-FO (Fig. 6.9b) for 2023 show ongoing losses of ice in the Amundsen Sea sector of WAIS, the same region where losses have been observed over the previous decade (e.g., Smith et al. 2020; Adusumilli et al. 2023). GRACE-FO data show a net mass loss over AIS between January 2023 and November 2023 of 170 Gt (red line in Fig. 6.10a), which was higher than the average annual mass loss of 100 Gt yr^{-1} between 2003 and 2023, and significantly different from the record-breaking 294 Gt mass gain that occurred in the previous year (2022). Monthly mass gains in 2023 were in part due to surface mass gains across Wilkes Land and Dronning Maud Land (see section 6c for surface mass balance details), which offset some of the large mass losses in coastal WAIS.

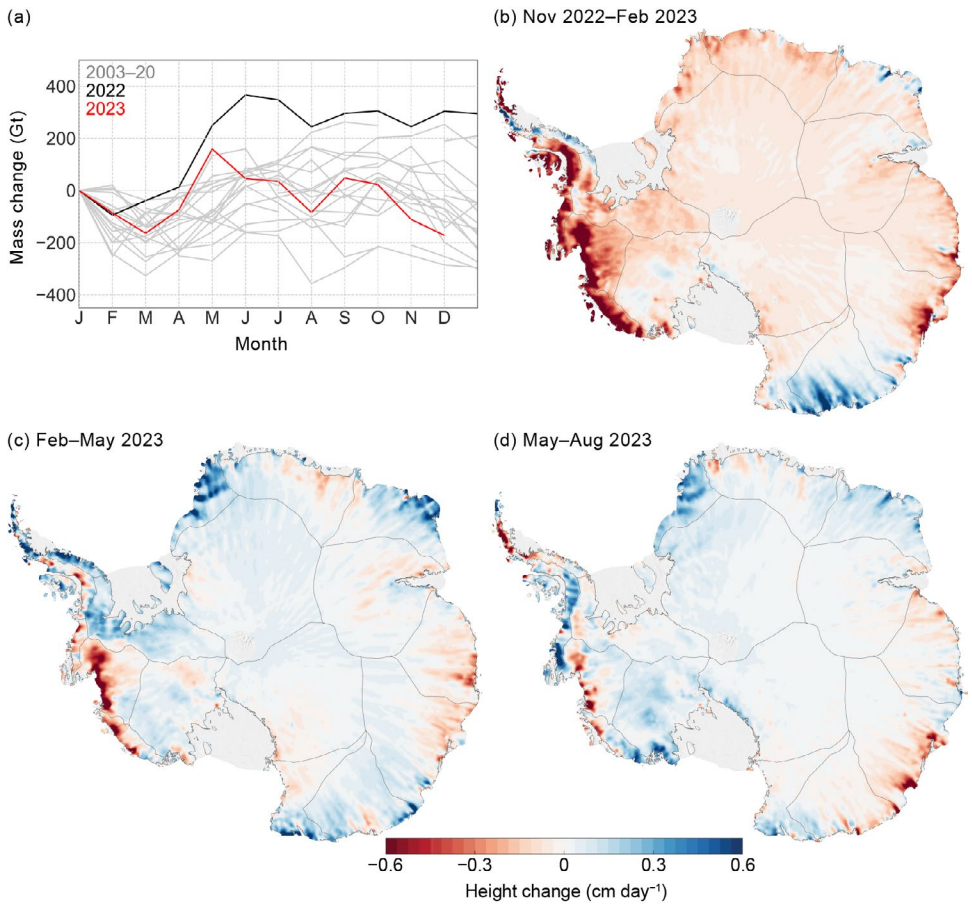

Fig. 6.10. (a) Time series of monthly mass changes (Gt) from GRACE and GRACE-FO, with 2022 and 2023 highlighted in black and red, respectively. Maps of height change (cm day^{-1}) from ICESat-2 shown at three-month intervals for (b) Oct–Dec 2022 to Jan–Mar 2023, (c) Jan–Mar 2023 to Apr–Jun 2023, and (d) Apr–Jun to Jul–Sep 2023. Dates inset on Fig. 6.10 represent the central month of each three-month ICESat-2 data acquisition cycle.

f. Sea-ice extent, concentration, and seasonality

—P. Reid, S. Stammerjohn, R. A. Massom, S. Barreira, T. A. Scambos, and J. L. Lieser

Net sea-ice extent (SIE; the area enclosed by greater than 15% sea-ice concentration) and sea-ice area (SIA; the product of sea-ice extent and concentration) were well below average or at record-low levels throughout 2023 (Fig. 6.11a). Monthly-mean low SIE and SIA records were significantly shattered for eight months in 2023 i.e., January, February, and May through October, and this is mirrored in the extreme curtailment of sea-ice growth around much of Antarctica during the autumn-winter advance season (Fig. 6.12a). The sea-ice deficit at a time of the year

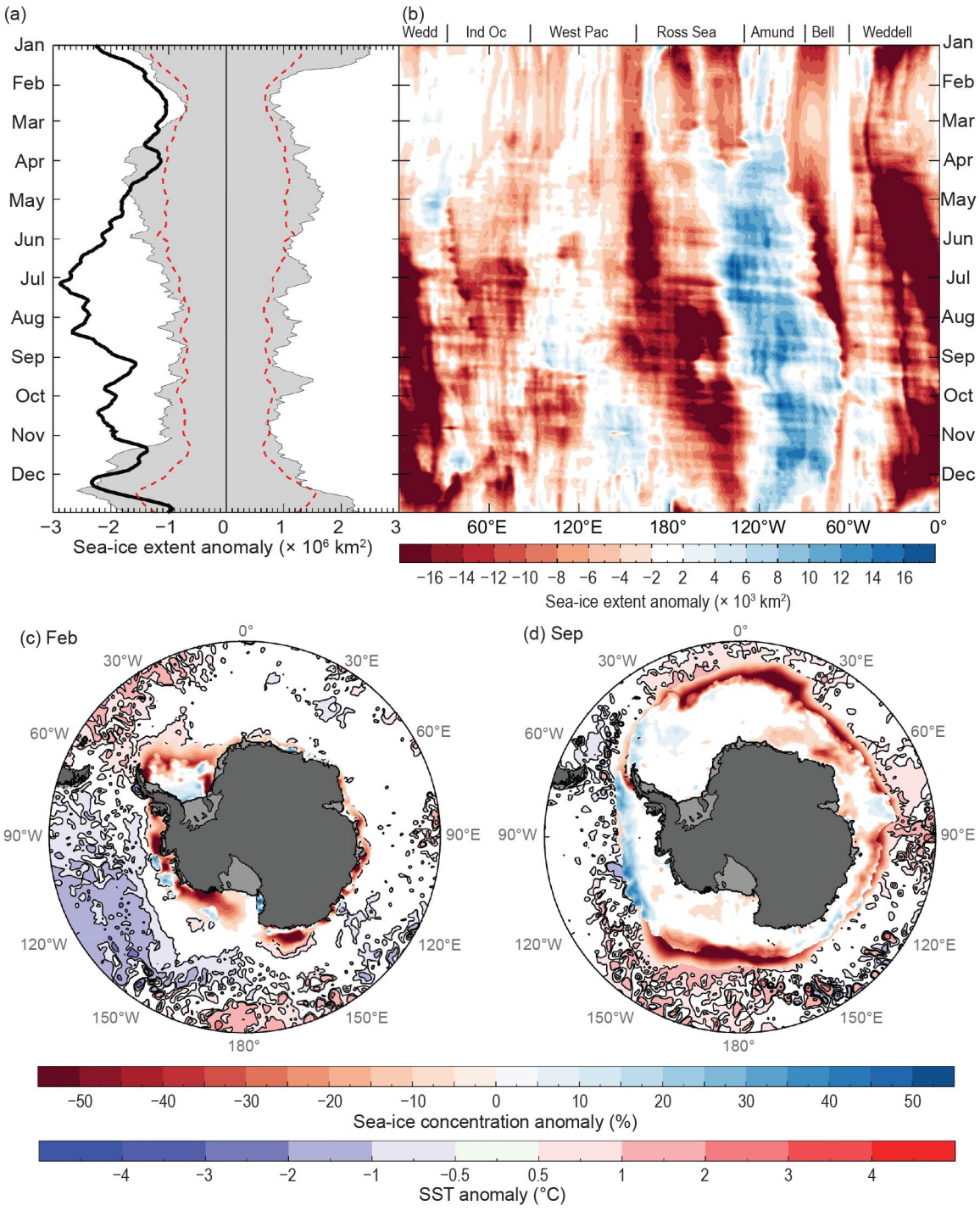

Fig. 6.11. (a) Time series of net daily sea-ice extent (SIE) anomaly (× 10^6 km²) for 2023 (solid black line; based on a 1991–2020 climatology). Gray shading represents historical (1979–2020) daily SIE anomaly, red dashed line represents ±2 std. dev., and (b) Hovmöller (time–longitude) representation of daily SIE anomaly (× 10^3 km² per degree of longitude) for 2023. (c),(d) Maps of sea-ice concentration anomaly (%) and sea-surface temperature (SST) anomaly (°C; Huang et al. 2020) for (c) Feb 2023 and (d) Sep 2023. Sea-ice concentration is based on satellite passive-microwave ice concentration data (Cavalieri et al. 1996, updated yearly for climatology; Maslanik and Stroeve 1999, for the 2023 sea-ice concentration). See Fig. 6.1 for relevant place names.

when the sea-ice zone should be growing is unprecedented in the satellite time series in both timing and magnitude. For example, net SIE was as much as ~2.9 × 10^6 km^2 below the long-term (1991–2020; used throughout) mean on 6 July, ~1.8 × 10^6 km^2 less than the previous record low for that date (in 2022; Reid et al. 2023). This situation is in contrast with the last seven years, starting with the first major downturn in Antarctic sea-ice coverage in 2016, when most record lows largely occurred during the late-spring through summer retreat/melt phase of the annual sea-ice cycle (Parkinson and DiGirolamo 2021). Regionally, SIE remained well below average almost everywhere apart from in the eastern Ross and Amundsen Seas for much of the year and in the Bellingshausen Sea for the second half of the year (Fig. 6.11b).

The unprecedented nature of Antarctic sea-ice coverage in 2023 is further highlighted by the 278 days (i.e., 76% of the entire year) and 245 days (67%) of record-low net daily SIE and SIA, respectively (Fig. 6.11a). The net daily SIE anomaly exceeded 2 std. dev. below the long-term mean throughout the entire year, apart from in late December. Moreover, the annual daily minimum SIE of 1.85 × 10^6 km^2 and SIA of 1.10 × 10^6 km^2 (both recorded on 21 February) were new all-time record lows, surpassing previous record-low annual minima set in 2022 (by 60,000 km^2 for SIE and 160,000 km^2 for SIA). Similarly, annual daily maximum SIE (of 17.00 × 10^6 km^2 on 7 September) and SIA (13.43 × 10^6 km^2 on 6 September) set new record lows and occurred two weeks earlier than normal.

Over the last eight years, 352 and 310 (out of 365) record-low daily values of SIE and SIA, respectively, have been broken. Despite the numerous record lows broken since 2016, but especially in 2023, it is worth noting that 1980 still retains a number of daily and monthly record lows (e.g., April for SIE and April–May for SIA).

Changes in upper-ocean conditions may be largely responsible for the increasing persistence in negative Antarctic SIE anomalies and reduced duration observed since 2016 (Cheng et al. 2022; Purich and Doddridge 2023; Hobbs et al., 2024). Although regional sea-ice anomalies can often be linked to regional atmospheric circulation anomalies (Massom et al. 2008), the persistence and wide distribution of negative SIE anomalies, as observed during 2022 and 2023 especially, point to circumpolar shifts in ocean–ice interactions. Within this context, the regional and temporal patterns and variations through 2023 are discussed below and closely reflect patterns and phenomena in the high-latitude atmospheric circulation and Southern Ocean (see sections 6b and 6g, respectively).

From January through March, Antarctic SIE was very much below average around most of the continent, except within small pockets of the Amundsen Sea and off Victoria Land within the western Ross Sea where SIE was slightly above average (Fig. 6.11b). Prior to this, in late 2022, a deep Amundsen Sea Low in the Pacific, contraction of circumpolar lows (associated with a strong polar vortex), and an associated strongly positive Southern Annular Mode (SAM) pattern enhanced advection of sea ice to more northerly latitudes and higher SSTs. This likely led to an early sea-ice retreat for 2022/23, setting the stage for the second consecutive record-low annual minimum. Negative SIE anomalies across parts of East Antarctica and most of the Ross and Bellingshausen Seas ranged between 1 std. dev. and 3 std. dev. below average, with the Bellingshausen Sea having persistently low SIE since August 2022 (see last year's report, Reid et al. 2023). During this time, above-average SSTs were present off Oates Land (~150°E–170°E) and within the Weddell Sea, with below-normal SSTs in the Ross, Amundsen, and Bellingshausen Seas (Fig. 6.11c; section 6g), while north of the Antarctic Circumpolar Current (ACC) there were extensive pools of anomalously high SSTs in the three major Southern Hemisphere basins (Indian, Atlantic, and western Pacific Oceans).

From April through August, sea ice advanced earlier than normal in only the Amundsen and eastern Ross Seas (Fig. 6.12a), consistent with the below-normal SSTs to the north of the ice edge in this region (see Fig. 6.13e). Regionally, sea ice within the eastern Ross Sea, at a deficit until the end of March, suddenly advanced quickly from April onwards (Fig. 6.11b), possibly as a result of the fresher-than-normal surface waters in that region (see Fig. 6.13f). Over these mid-autumn through winter months, net SIE was substantially below average (Fig. 6.11a), with substantial parts of the Ross and Weddell Seas being over 6 std. dev. below daily average during July and August. Notably, the largest SIE anomalies were region-specific and centered on the Indian Ocean sector of East Antarctica (~30°E–90°E), the western Pacific to Ross Sea (~150°E–130°W),

and the Bellingshausen and Weddell Seas (~80°W–10°E). In these regions, lack of typical annual sea-ice advance (Fig. 6.12a) and the subsequent major deficit in sea-ice coverage through winter coincided with above-normal SSTs (by ~2°C; Fig. 6.11c) in each of the three ocean basins, stretching poleward across the ACC, with the anomalously high SSTs and upper-ocean temperatures delaying sea-ice growth and intensifying the negative SIE anomalies in the Indian, Atlantic, and western Pacific sectors in late June through early July (Fig. 6.11b). During August, as a positive pressure/anticyclonic circulation anomaly developed over the Ross-Amundsen Seas region, consistent with the onset of El Niño (see section 6b), there was a sudden growth of sea ice within the Bellingshausen Sea such that SIE changed from well below to slightly above average by the end of August, with this pattern continuing through November.

By the start of September, SSTs that were above normal by as much as 2°C, largely encircled the sea-ice edge (Fig. 6.11d). A marked change occurred in the atmospheric synoptic pattern, whereby anomalous high pressure that had been observed in the Ross Sea during July and August migrated east into the Bellingshausen Sea in September to be replaced by a deep low-pressure system in the Ross Sea (not shown but see Fig. 6.3e). This change brought about a burst of sea-ice growth in the western Ross Sea, reducing the magnitude of the anomalously low SIE in that region while simultaneously reducing the SIE across East Antarctica (~90°E–120°E). Anomalous low pressure also developed briefly in the Weddell Sea during October and enhanced sea-ice growth in the Bellingshausen and western Weddell Seas. Thus, SIE within the western Pacific retreated slowly from September to November (Fig 6.12b), albeit from a very low extent, so that by the end of November the SIE within this region was close to its long-term average. Elsewhere, the SIE anomaly pattern remained reasonably static from September through November, with very low SIE across much of East Antarctica and the eastern Ross and Weddell Seas.

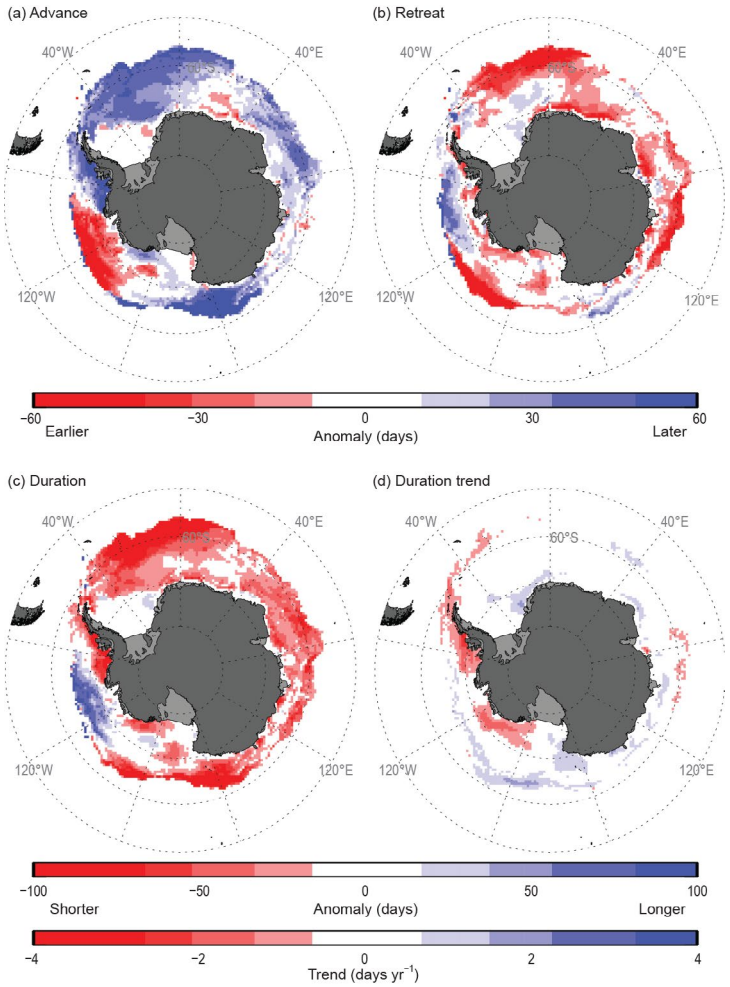

Fig. 6.12. Maps of seasonal sea-ice anomalies (days) in 2023 during (a) autumn ice-edge advance, (b) spring ice-edge retreat, and (c) winter ice-season duration; together with (d) winter ice-season duration trend (days yr^{-1}; Stammerjohn et al. 2008). The seasonal anomalies (a)–(c) are computed against the 1991/92 to 2020/21 climatology; the trend (d) is computed over 1979/80–2023/24. The climatology (for computing the anomalies) is based on data from Comiso (2017; updated yearly), while the 2023/24 ice-edge retreat duration-year data are from the NASA Team NRTSI dataset (Maslanik and Stroeve 1999); the trend is based on the merged dataset containing 1979–2022 data from Comiso (2017) and 2023/24 data from the NASA Team NRTSI dataset (Maslanik and Stroeve 1999).

December saw an intensification of the circumpolar westerlies (section 6b) leading to a distinct change in the regional SIE anomaly. Notable during this month was the formation of two deep low-pressure anomalies (see Fig. 6.3g). One, to the north of the sea-ice edge in the Weddell Sea (~20°W), appears to have initially caused a reduction in regional SIE and a coincident compaction of the sea-ice zone by northerly winds (cf. Massom et al. 2008) within the central Weddell Sea. This led to persistence of a broad band of high-concentration ice in the eastern Weddell Sea (from ~0° to 30°W) and slower-than-normal sea-ice retreat there during December (Fig. 6.12b). The other negative pressure anomaly was centered to the south of the ice edge in the Ross Sea, slowing seasonal sea-ice retreat off Oates Land and parts of the Ross Sea (~150°E–150°W).

In terms of seasonality, records were broken across most Antarctic sectors, with greater than two-month delays in the ice edge advance and greater than two-month earlier ice edge retreat (Figs. 6.12a,b). Regional exceptions during the autumn advance were the western Bellingshausen, Amundsen, and eastern Ross Seas (~90°W–150°W) and the Bellingshausen-Amundsen Seas (~60°W–120°W) during the retreat. Taken together, 2023 was marked by the largest and most widespread decreases in ice-season duration (Fig. 6.12c) yet observed since 1979, with most regions experiencing a three-to-four-month shorter ice season, the only exception being the western Bellingshausen and eastern Amundsen offshore areas (~80°W–120°W). Anomalously low coverage of sea ice in 2023 also resulted in 154 days of record-high coastal exposure (i.e., total lack of a protective sea-ice "buffer" offshore; Reid and Massom 2022), with implications for ice-shelf stability (Massom et al. 2018; Teder et al. 2022). This occurred mostly during the late 2022/23 retreat and early advance periods, with many days having more than twice the usual coastal exposure.

The recent abrupt switch from record and near-record high SIE in 2012–14 and the first half of 2015 to record lows after 2016 indicates a potential transition in the Southern Ocean–ice–atmosphere system. After nearly four decades of gradual increase in net SIE, unreconciled with climate models that predict general Antarctic sea-ice decline with an increasingly warmer global climate, it is now plausible that oceanic and atmospheric warmth have begun to transform the Southern Ocean system and that non-linear feedbacks may have been activated.

g. Southern Ocean

—S. Thomalla, R. L. Beadling, M. du Plessis, E. Souza, D. Fernandez, S. T. Gille, S. A. Josey, G. A. MacGilchrist, A. Marouchos, C. R. McMahon, L. Pezzi, C. Schultz, J.-R. Shi, S. C. Tripathy, and K. Turner

The Southern Ocean (SO) plays a critical role in buffering the impacts of climate change by accounting for 50% of the oceanic uptake of anthropogenic carbon dioxide (CO_2) and 75% of the oceanic uptake of anthropogenic heat (Frölicher et al. 2015). Physical processes influence air–sea exchanges of heat, while carbon fluxes are additionally strongly affected by biological processes. Both physical and biological processes exhibit seasonal, inter-annual, and decadal variability, reflecting large-scale responses to atmospheric drivers, all of which affect the transfer of carbon and heat with complex feedbacks on ocean biogeochemistry and climate (Henley et al. 2020). Here, we assess the 2023 anomalies in key physical and biological SO metrics. Results for 2023 are intriguing in the context of the record-low sea-ice coverages discussed in section 6f that may reflect alterations in the underlying processes that determine the state of sea-ice (Purich and Doddridge 2023). Key outcomes highlight substantial ocean warming with a dominance of SO positive anomalies in sea-surface temperature (SST), ocean heat content (OHC), and air–sea heat flux. Such changes may be exacerbated by the warm conditions of the 2023 El Niño, with evidence of cascading impacts on ocean biogeochemistry. These results highlight the impact of changing atmosphere–ocean dynamics that are of particular concern given the central role that the SO exerts on the climate system.

1. SEA-SURFACE TEMPERATURE, SALINITY, AND MIXED-LAYER DEPTH

Sea-surface temperature anomalies for 2023 (relative to 2004–20) were determined from NOAA OI SST V2 (Reynolds et al. 2002). Positive SST anomalies across much of the SO (Fig. 6.13a) revealed warming (up to 1.5°C). Overall, the SO remained warmer than normal throughout the year (Fig. 6.13e), following the warming tendency in previous years (Beadling et al. 2022; Pezzi et al. 2023). A notable exception is the eastern Pacific sector, which revealed negative anomalies (up to −0.8°C; Fig. 6.13a) particularly in late summer (February–April; Fig. 6.13e). The Pacific temperature anomaly dipole in 2023 reflects the emergence of a positive pressure/anticyclonic anomaly over the high-latitude South Pacific associated with the transition to El Niño (section 6b). Anomalies of sea-surface salinity (SSS) derived from the Argo dataset (Roemmich and Gilson 2009) relative to the 2004–18 climatology were similar to 2022 values discussed in last year's report (Pezzi et al. 2023), with positive anomalies (up to 0.12 PSU) dominating large parts of the SO (Fig. 6.13b), especially in winter and spring with the most extreme positive anomalies occurring in the Atlantic sector (Fig. 6.13f). The SO overall expressed a slight negative SSS anomaly in late summer (January–April) due predominantly to anomalies in the Indian basin (Fig. 6.13f). The annual anomaly in mixed-layer depth (MLD, defined according to de Boyer Montégut et al. [2004] applied to Argo) relative to 2004–22 is dominated by wintertime anomalies and characterized by negative (shallower) MLDs in the western Pacific and central Indian Ocean sectors interspersed with positive (deeper) MLDs in the eastern Pacific and Indian up to ±~80 m (Figs. 6.13c,g). In contrast, 2022 was characterized by deeper MLD anomalies over the majority of the SO (including both western and eastern Pacific and the central Indian) with only a small negative anomaly within the eastern Indian sector. The zonal dipole in Pacific MLD anomalies (Fig. 6.13c) reflects that of SST, with warmer anomalies in the western Pacific aligned with shallower winter MLDs, while cooler SST anomalies in the eastern Pacific are associated with deeper winter MLDs (Figs. 6.13a,c).

2. AIR–SEA HEAT FLUX

Net heat-flux anomalies for 2023 (relative to 1998–22) were derived from the ERA5 reanalysis (Hersbach et al. 2020). The effects of positive pressure anomaly in the South Pacific associated with El Niño are similarly present in the net heat-flux pattern (Fig. 6.13d), with positive anomalies (less heat loss from the ocean) dominating in the western Pacific (synchronous with high SST and shallow winter MLD) and negative anomalies (more heat loss from the ocean) in the eastern Pacific. The seasonal cycle of anomalies (Fig. 6.13h) suggests that these effects are most prominent in winter when the positive pressure anomalies are strongest (see Fig. 6.3e). The SO heat-flux asymmetry index (Josey et al. 2023), which measures the difference in Atlantic–Indian and

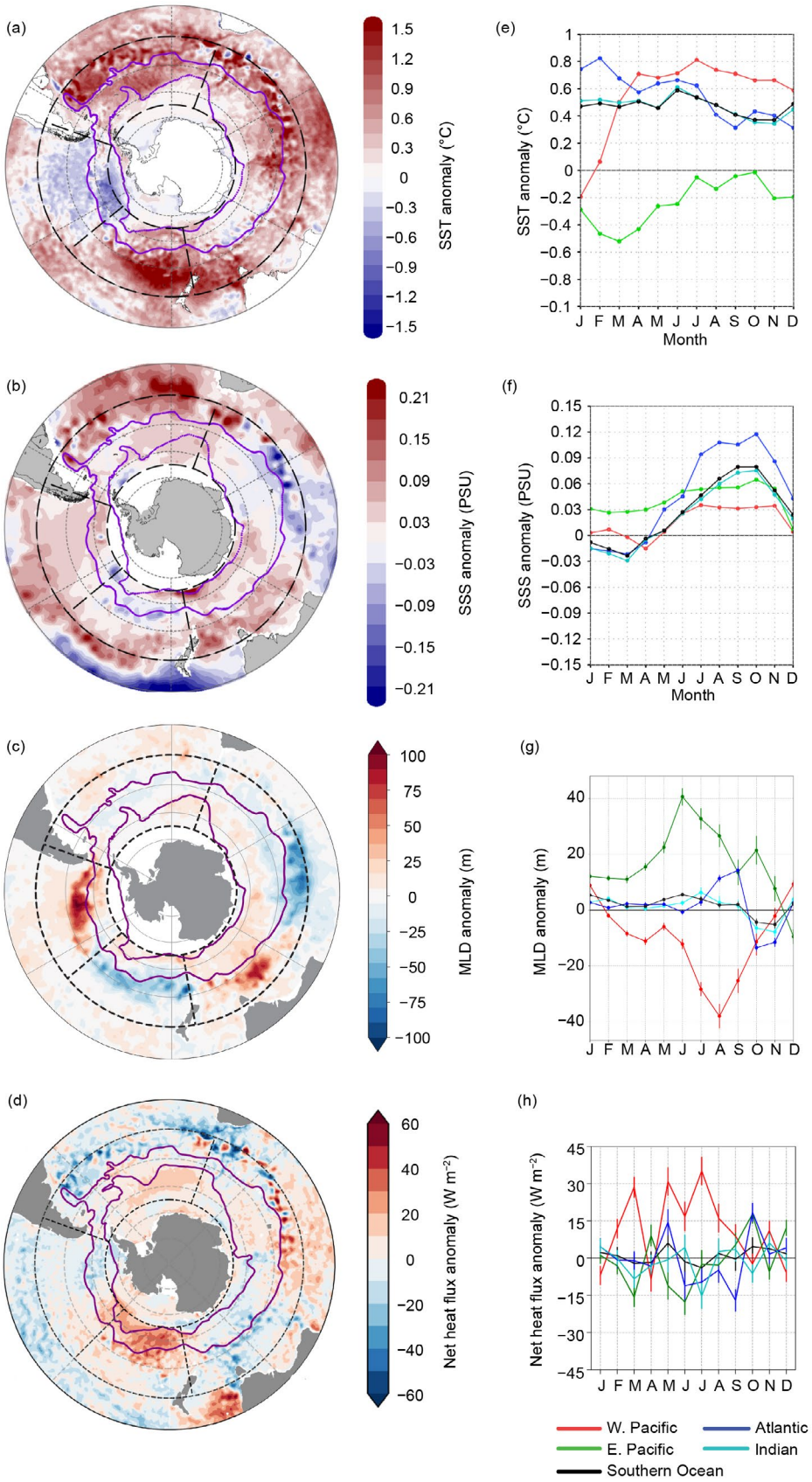

Fig. 6.13. Annual-average anomalies (Jan–Dec 2023) of (a) sea-surface temperature (SST; °C), (b) sea-surface salinity (SSS; PSU), (c) mixed-layer depth (MLD; m), and (d) net heat flux (W m^{-2}). Overlaid are the positions of the Subantarctic and Southern Boundary Antarctic Circumpolar Fronts (purple lines) as defined by Orsi et al. (1995). Four distinct regions between 40°S and 65°S are delineated by black dashed contours corresponding to the Atlantic (70°W–20°E), Indian (20°E–170°E), western Pacific (170°W–120°W), and eastern Pacific (120°W–70°W) sectors. The 2023 seasonal cycle of anomalies in (e) SST (°C), (f) SSS (PSU), (g) MLD (m), and (h) net heat flux (W m^{-2}) separated according to the four sectors defined above. Error bars in (g),(h) represent the standard error of the climatological mean (i.e., std. dev. divided by √N, where N is the number of years, the number of years in the climatology).

Pacific sector surface heat exchange, was –1.48 in 2023, which reflects a weakening of the asymmetry that is commonly seen during El Niño.

3. UPPER OCEAN HEAT CONTENT

The 0-m–2000-m OHC was retrieved from monthly gridded Argo temperature data (Roemmich and Gilson 2009), with 2023 anomalies determined relative to 2005–20 climatology. The annual OHC anomaly (Fig. 6.14a) gained heat with positive anomalies to the north of the Antarctic Circumpolar Current (ACC). The OHC cooling anomalies east of Australia and within the ACC of the eastern Pacific, in addition to the patchy cooling evident in the Indian sector east of South Africa, typically align with negative SST anomalies (Fig. 6.13a). The OHC anomaly time series shows a long-term warming since 2005 (Fig. 6.14b). Although globally the 0-m–2000-m OHC in 2023 exceeded that of 2022 by around 10 ZJ (Cheng et al. 2024), the SO shows a decrease in OHC (–1.0 ZJ) in 2023 relative to 2022 (Fig. 6.14b).

4. OCEAN BIOGEOCHEMISTRY

Chlorophyll data from the eight-day European Space Agency Ocean Colour Climate Change Initiative (OC-CCI) product (v6.0; Sathyendranath et al. 2019) were processed as per Thomalla et al. (2023), with 2023 anomalies computed relative to 1999–2023 climatology (Fig. 6.14c). For the SO as a whole, chlorophyll shows a typical alignment with the long-term average during winter, spring, and autumn, but a strong positive anomaly during the summer bloom. The positive anomaly in summer chlorophyll was dominated by the eastern Pacific, which coincided with cooler SSTs, negative heat-flux anomalies, and deeper MLDs (Figs. 6.13a,c,d). Conversely, the

western Pacific expressed negative chlorophyll anomalies in both spring and late summer aligned with higher SSTs, positive heat flux, and shallower MLDs (Figs. 6.13a,c,d). Anomalies in dissolved oxygen (DO) for 2023 relative to 2003–22 climatology were derived per ocean basin from Biogeochemical Argo (BGC-Argo; Wong et al. 2020; Fig. 6.14d). The Pacific dipole is similarly reflected in DO with negative 0-m–250-m anomalies in the western Pacific, consistent with warmer waters, shallower mixed layers, and below-average chlorophyll concentrations, while in the eastern Pacific the opposite occurred (with the positive DO anomaly particularly evident at 150-m–300-m depth). The most distinctive feature in DO was a strong negative anomaly in the top ~250 m in the Atlantic, which aligned with pronounced positive anomalies in SST, SSS, and OHC (Figs. 6.13a,b; Fig. 6.14a), despite positive anomalies in chlorophyll (Fig. 6.14c).

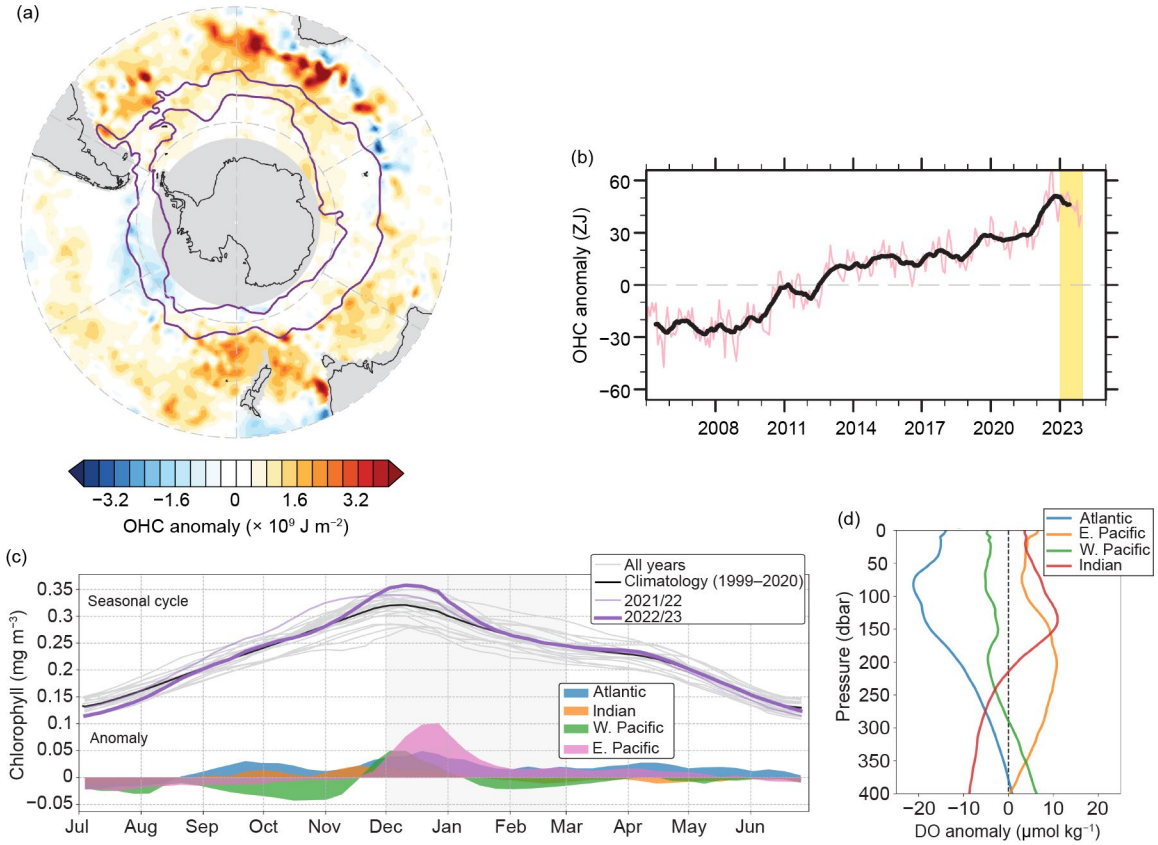

Fig. 6.14. (a) 2023 annual average ocean heat content (OHC; × 10^9 J m^{-2}) anomalies. Overlaid are the Subantarctic and Southern Boundary Antarctic Circumpolar Fronts (purple lines) as defined by Orsi et al. (1995). (b) Time series of monthly average 0-m–2000-m OHC anomaly (ZJ or 10^{21} J) relative to 2005–20 Argo climatology south of 30°S (red line) with 12-month running mean on top (black line) and 2023 highlighted (yellow shading). (c) Seasonal cycle of area-weighted (40°S–65°S) daily-mean chlorophyll concentration (mg m^{-3}) depicting all historical years (gray lines), the climatological 1999–2023 mean (black line), and the most recent two growing seasons (purple lines); anomalies for Jul 2022–Jun 2023 relative to the 1999–2023 climatological mean are depicted for each ocean sector (colored shading). (d) Dissolved oxygen (DO) anomalies (kg m^{-3}) with pressure (dbar) for Jul 2022–Jun 2023 relative to the 2005–20 Argo climatology.

h. 2023 Antarctic ozone hole

—N. A. Kramarova, P. A. Newman, L. R. Lait, B. Johnson, M. Pitts, M. L. Santee, I. Petropavlovskikh, L. Coy, and J. De Laat

The 2023 Antarctic ozone hole was the 16th largest in 44 years of satellite observations since 1979, with an average area of 23.08 × 10^6 km^2 (averaged for 7 September–13 October) and a minimum daily total ozone column of 99 Dobson Units (DU; 1 DU is equivalent to a layer of pure ozone 0.01 mm thick at standard temperature and pressure) on 3 October. The 2023 Antarctic ozone hole appeared earlier than in recent years and exceeded 20 × 10^6 km^2 by 2 September. In early September—a critical period for ozone depletion—lower stratospheric temperatures were below average. A strong wave event warmed the lower stratosphere by 6.1 K and reduced the ozone hole area by 4.9 × 10^6 km^2 between 17 and 28 September. Meteorological conditions in the lower Antarctic stratosphere and the area of the ozone hole were close to average from late September to mid-November. Weak wave activity in late austral spring slowed the seasonal transition to summer, similar to the situation in the three previous years (2020, 2021, and 2022). As a result, lower stratospheric temperatures were below average and the ozone hole persisted longer than normal in 2023, breaking up on 20 December (the 1990–2019 average breakup date is 9 December).

In January 2022, the Hunga volcano (previously referred to as Hunga Tonga–Hunga Ha'apai) injected volcanic material (e.g., Carr et al. 2022; Taha et al. 2022) and a record amount of water vapor (~146 ±5 Tg) directly into the stratosphere (e.g., Millán et al. 2022; Blunden et al. 2023), increasing global stratospheric water vapor by ~10%. In 2022, Hunga volcanic aerosols and excess water vapor did not penetrate into the southern stratospheric vortex (Manney et al. 2023) and therefore did not directly affect the 2022 ozone hole development and the chemical composition inside the Antarctic vortex (Kramarova et al. 2023).

Following the 2022 Southern Hemisphere (SH) vortex breakup, the Hunga plume was advected to Antarctic polar latitudes (Manney et al. 2023; Santee et al. 2024). Water vapor observations in May and the first half of June 2023 (Fig. 6.15b) showed a 25%–50% increase above average on the 440-K isentropic surface (~60 hPa or ~19 km). Excess moisture shifted the threshold temperatures for polar stratospheric cloud formation upward by ~1 K–2 K (Santee et al. 2024). Antarctic lower stratospheric temperatures were near average in May and dropped to below average in June (Fig. 6.15a). The combination of colder temperatures and excess water vapor in the stratosphere facilitated earlier-than-usual polar stratospheric cloud formation (Fig. 6.15d) over an extended vertical range. Polar stratospheric clouds provide surface area for heterogeneous reactions that convert reservoir chlorine species into active forms (e.g., chlorine monoxide [ClO]; Fig. 6.15c) that can catalytically destroy ozone. The record-high polar stratospheric cloud volume in May and June (Fig. 6.15d) resulted in unusually early chlorine activation in the Antarctic stratosphere (Santee et al. 2024), particularly at higher altitudes near 600 K–800 K (not shown). However, while unprecedented, this early winter chlorine activation was much weaker than that occurring later in the season and did not induce substantial ozone depletion.

Seasonal dehydration—the process whereby water vapor concentrations decline in the polar lower stratosphere every year due to sedimentation of ice polar stratospheric particles—occurred at higher altitudes, and the amount of water vapor removed was also higher than average (Santee et al. 2024). The sharp peak in water vapor mixing ratios (above the already-elevated values) evident in late May on the 440-K surface (Fig. 6.15b) is likely a signature of rehydration from evaporation of ice polar stratospheric cloud particles sedimenting from above. Water vapor dropped to below-average levels on this surface by the end of June (Fig. 6.15b) and then stayed near the average until December.

In 2023, chlorine activation, represented by ClO (Fig. 6.15c), lasted longer than usual, reaching its maximum in the second half of September (a critical period for ozone depletion). Because of the Montreal Protocol (World Meteorological Organization 2022), chlorine and bromine concentrations in the Antarctic stratosphere are slowly declining. Effective equivalent stratospheric chlorine (EESC, a metric for the abundance of chlorine and bromine species; Newman et al.

2007) levels in 2023 were around 3.23 ppbv, ~15% lower than the maximum values observed in the early 2000s. The EESC decline resulted in lower ClO concentrations in 2023 compared to those in 2006. The 2023 ozone depletion between early July and early October was about 2.18 ppmv, smaller than the 2.24 ppmv ozone depletion in 2006 when the stratospheric ClO concentration in September was a record high.

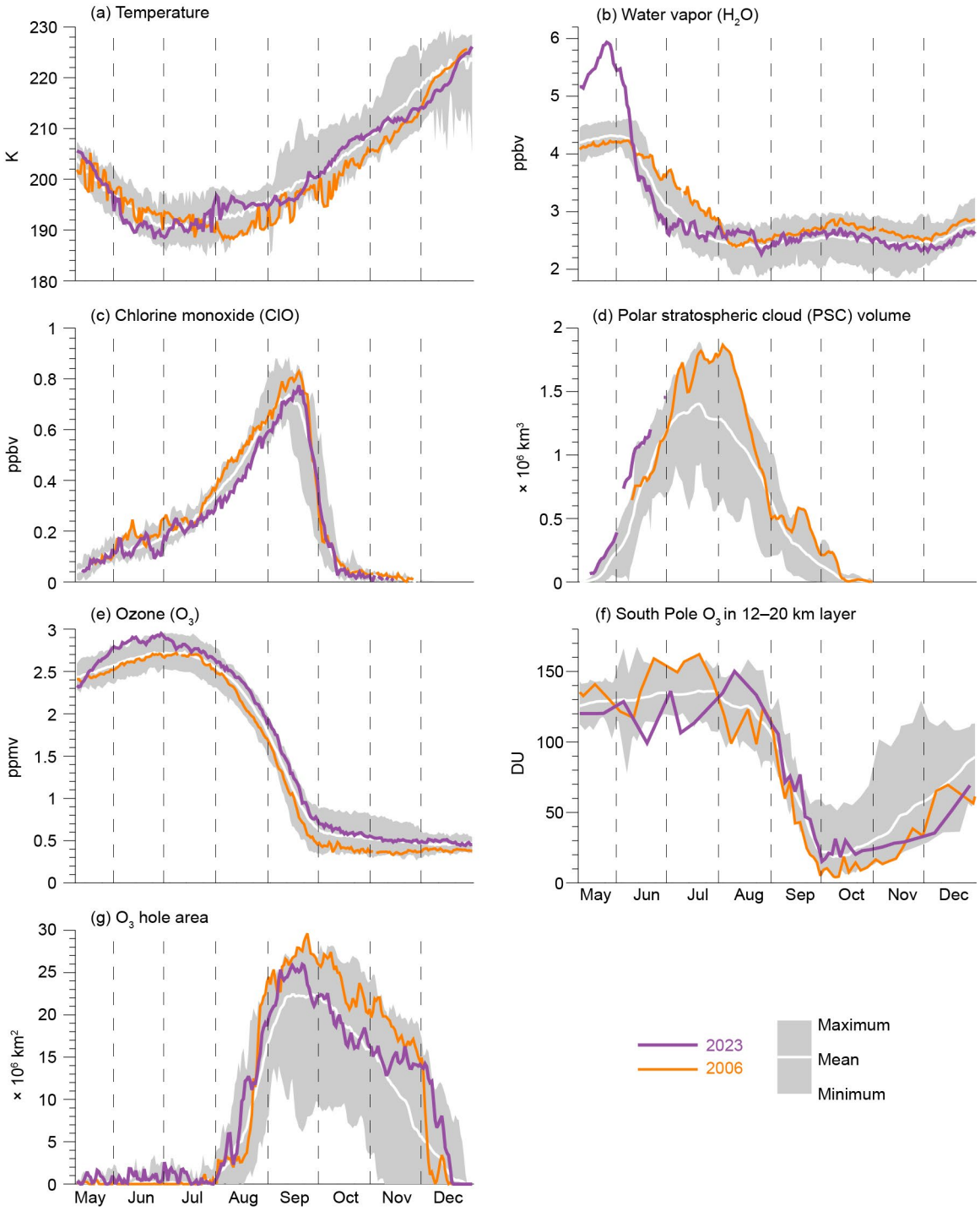

Fig. 6.15. Antarctic values of (a) vortex-averaged MERRA-2 temperature (K) on the 440-K potential temperature surface (~19 km or 60 hPa, vortex-averaged), (b) H_2O (ppmv), (c) ClO (ppbv), and (e) O_3 (ppmv) on the 440-K potential temperature surface from Aura MLS (updated from Manney et al. 2011), (d) CALIPSO polar stratospheric cloud (PSC) volume (× 10^6 km^3) updated from Pitts et al. 2018), (f) lower stratospheric ozone columns (12 km–20 km; DU) based on sonde measurements at South Pole, (g) Ozone Monitoring Instrument (OMI)/Ozone Mapping and Profiler Suite (OMPS) Antarctic ozone hole area (× 10^6 km^2; area with ozone total column less than 220 DU). Gray shading shows the range of daily Antarctic values for 2005 (for all but [d], which starts in 2006) through 2022. The white curve indicates the 2005–22 long-term mean. CALIPSO measurements ceased at the end of June 2023.

Lower stratospheric ozone column between 12 km and 20 km derived from sonde measurements at South Pole (SP) station was near or below average during May–July 2023 (Fig. 6.15f) and then above average in August. SP columns quickly declined in September, reaching the minimum value of 15.3 DU on 1 October. The Antarctic ozone hole area—the area with total ozone columns below 220 DU—appeared earlier than in recent years (Fig. 6.15g) and reached its peak on 21 September at 25.96 × 10^6 km^2. The area of the ozone hole was then sharply reduced by 4.9 × 10^6 km^2 following the mid-September warming event (Fig. 6.15a). Another strong wave event in early October kept temperatures, ozone hole area, and SP columns near average in October and early November. From mid-October, the planetary-scale wave activity was very low, coinciding with the strong polar vortex (section 6b), resulting in a delayed vortex breakup (winter-to-spring transition) as in the previous three years (2020–22). Weaker wave activity kept the ozone hole area larger and the SP column and stratospheric temperatures lower than usual from mid-November through December (Figs. 6.15a,f,g).

Reduced ozone depletion due to declining EESC is observable on decadal timescales (Fig. 6.16), with year-to-year hole variations modulated by Antarctic lower stratospheric temperatures. The relationship between September lower stratospheric temperatures and area deviations in September, obtained by fitting a quadratic function of EESC with a 5.2-year mean age (shown as a gray line in Fig. 6.16a) to the observed ozone hole areas, reveals that ozone holes are larger in colder-than-average years (Fig. 6.16b). Model simulations (e.g., Fleming et al. 2024) suggest that excess water vapor should lead to an additional 10 DU–20 DU ozone depletion, thereby increasing ozone hole area by ~1 × 10^6 km^2 to 3 × 10^6 km^2, but such an increase is difficult to detect because of the natural year-to-year variability of ~4 × 10^6 km^2 (Newman et al. 2004). The 2023 ozone hole lasted longer than usual (Fig. 6.16c). The 2023 November hole severity can be explained by

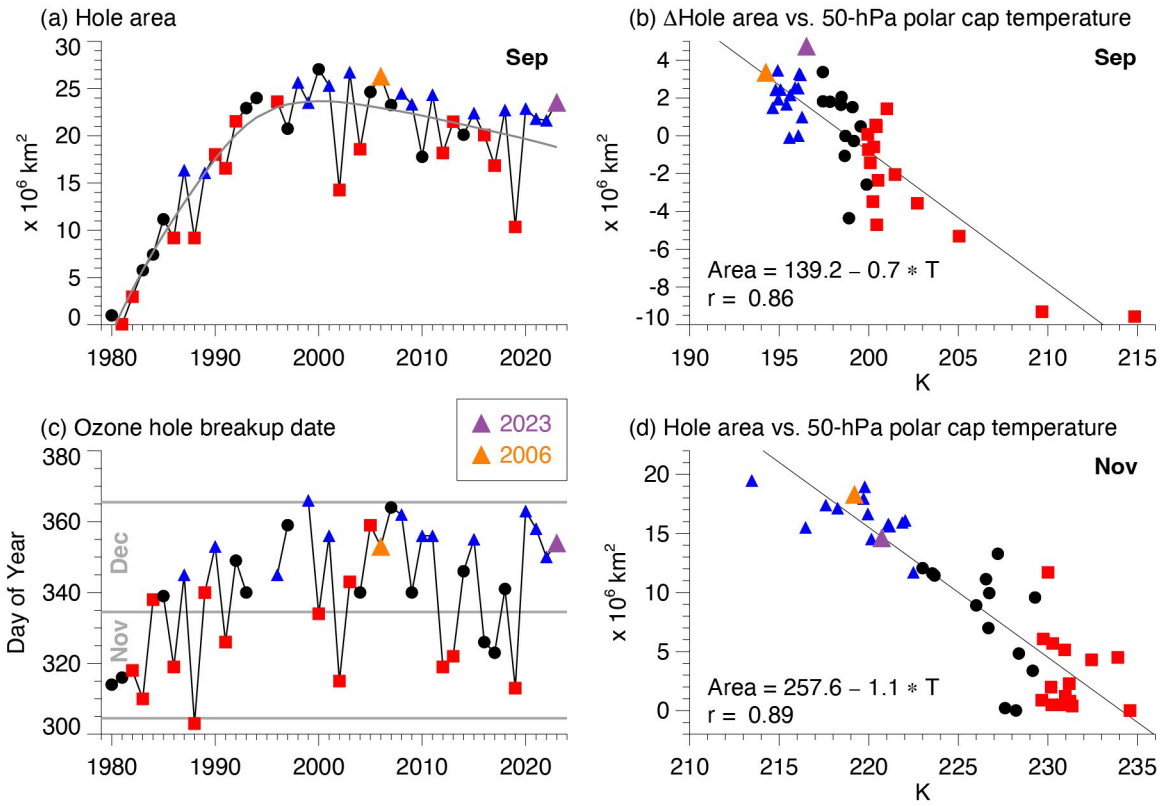

Fig. 6.16. (a) Sep average Antarctic ozone hole area. (b) Sep anomalies of the ozone hole area (see text) vs. MERRA-2 Sep 50-hPa temperatures averaged over the polar cap (60°S–90°S). (c) Ozone hole disappearance dates. (d) Nov ozone hole areas vs. MERRA-2 Nov 50-hPa temperatures. In (a), the gray curve shows a quadratic fit of effective equivalent stratospheric chlorine with a 5.2-year mean age of air (Newman et al. 2007) to the Sep hole areas. Years with temperatures in the lowest (highest) third are shown as blue triangles (red squares), and the years 2006 and 2023 are highlighted in orange and purple, respectively. Ozone data for 1979–92 are from Total Ozone Mapping Spectrometer (TOMS) Nimbus-7, 1993–94 are from TOMS Meteor-3, 1996–2004 are from TOMS-Earth Probe, 2005–15 are from Aura Ozone Monitoring Instrument (OMI), and 2015–23 are from Suomi National Polar-orbiting Partnership (SNPP) Ozone Mapping and Profiler Suite (OMPS). There were no satellite total ozone observations for 1995.

below-average stratospheric temperatures (Fig. 6.16d) due to weak wave activity in late austral spring. This weaker-than-average wave activity slowed the winter-to-summer transition, resulting once again in a longer-lasting ozone hole, similar to the behavior in 2020, 2021, and 2022.

Despite exceptional water vapor from the Hunga eruption and earlier onset of chlorine activation at the beginning of austral winter, the 2023 Antarctic ozone hole was quite ordinary. The levels of active chlorine in 2023 and seasonal ozone losses were smaller than in 2006 due to the Montreal Protocol and consistent with our understanding of polar ozone depletion. The excess water vapor may have caused some small additional ozone depletion particularly early in the season, but the losses are too small to decisively isolate and estimate the Hunga contribution to the 2023 Antarctic ozone hole.

Acknowledgments

- L. P. Pezzi acknowledges support from PROANTAR's Antarctic Modeling and Observation System (ATMOS) Project under the CNPq/PROANTAR award 443013/2018-7.
- S. A. Josey acknowledges funding from the European Union Horizon 2020 research and innovation programme under grant agreement no. 821001 SO-CHIC.
- S. T. Gille received support from NSF Award OPP-1936222.
- S. J. Thomalla acknowledges institutional support from the CSIR Parliamentary Grant (0000005278) and the Department of Science and Innovation.
- K. R. Clem acknowledges support from the Royal Society of New Zealand Marsden Fund grant MFP-VUW2010.
- D. E. Mikolajczyk, L. M. Keller, T. P. Norton, and M. A. Lazzara thank the support of the US National Science Foundation, Office of Polar Programs, grants #2301362, 1924730, and 1951603.
- Work at the Jet Propulsion Laboratory, California Institute of Technology, was done under contract with the National Aeronautics and Space Administration (NASA). Support was also provided by the NASA Modeling and Analysis Program. We are indebted to the many NOAA Corps Officers and GML technical personnel who spend the winters at South Pole Station to obtain the ongoing balloon and ground-based data sets. We also acknowledge the logistics support in Antarctica provided by the National Science Foundation Office of Polar Programs. © 2024. All rights reserved.
- P. Reid and J. Lieser were supported through the Australian Bureau of Meteorology, and R. Massom by the Australian Antarctic Division. The work of P. Reid and R. Massom also contributes to the Australian Government's Australian Antarctic Partnership Program (AAPP). For R. Massom, this work was also supported by the Australian Research Council Special Research Initiative the Australian Centre for Excellence in Antarctic Science (Project Number SR200100008).
- S. Stammerjohn was supported under NSF PLR–1552226; she also thanks the Institute of Arctic and Alpine Research and the National Snow and Ice Data Center, both at the University of Colorado Boulder, for institutional and data support.
- L. D. Trusel and J. D. Kromer acknowledge support from the NASA Cryospheric Sciences Program award 80NSSC$_{20}$K0888.

Appendix 1: Acronyms

ACC	Antarctic Circumpolar Current
AIS	Antarctic ice sheet
AR	atmospheric river
ATLAS	Advanced Topographic Laser Altimeter System
AWS	automatic weather station
BGC	biogeochemical
ClO	chlorine monoxide
CRI	coastal resolution improvement
DMSP	Defense Meteorological Satellite Program
DO	dissolved oxygen
DU	Dobson Units
EESC	effective equivalent stratospheric chlorine
ERA5	European Centre for Medium-Range Weather Forecasts Reanalysis version 5
GRACE	Gravity Recovery and Climate Experiment
GRACE-FO	Gravity Recovery and Climate Experiment Follow-on
H_2O	water
IceSat-2	Ice, Cloud and Land Elevation Satellite
MAR	Modèle Atmosphérique Régional
MERRA-2	Modern-Era Retrospective Analysis for Research and Applications version 2
MLD	mixed layer depth
MLS	Microwave Limb Sounder
NSIDC	National Snow and Ice Data Center
O_3	ozone
OC-CCI	Ocean Colour Climate Change Initiative
OHC	ocean heat content
OMI	Ozone Monitoring Instrument
OMPS	Ozone Mapping and Profiler Suite
PSC	polar stratospheric cloud
SAM	Southern Annular Mode
SH	Southern Hemisphere
SIA	sea-ice area
SIE	sea-ice extent
SMB	surface mass balance
SMMR	Scanning Multi-Channel Microwave Radiometer
SO	Southern Ocean
SP	South Pole
SSM/I	Special Sensor Microwave Imager
SSMIS	Special Sensor Microwave Imager/Sounder
SSS	sea-surface salinity
SST	sea-surface temperature
TOMS	Total Ozone Mapping Spectrometer
WAIS	West Antarctic Ice Sheet

Appendix 2: Datasets and sources

Section 6b Atmospheric circulation and surface observations

Sub-section	General Variable or Phenomenon	Specific dataset or variable	Source
6b	Modes of Variability	Marshall Southern Annular Mode Index	http://www.nerc-bas.ac.uk/icd/gjma/sam.html
6b	Temperature, [Near] Surface	ERA5	https://www.ecmwf.int/en/forecasts/dataset/ecmwf-reanalysis-v5
6b	Geopotential Height	ERA5	https://www.ecmwf.int/en/forecasts/dataset/ecmwf-reanalysis-v5
6b	Pressure, Sea Level or Near-Surface	ERA5	https://www.ecmwf.int/en/forecasts/dataset/ecmwf-reanalysis-v5
6b	Pressure, Sea Level or Near-Surface	University of Wisconsin Madison automatic weather stations - Antarctic Meteorological Research and Data Center	https://amrdcdata.ssec.wisc.edu
6b	Pressure, Sea Level or Near-Surface	Staffed weather station data	https://legacy.bas.ac.uk/met/READER/
6b	Temperature, [Near] Surface	University of Wisconsin Madison automatic weather stations - Antarctic Meteorological Research and Data Center	https://amrdcdata.ssec.wisc.edu
6b	Temperature, [Near] Surface	Staffed weather station data	https://legacy.bas.ac.uk/met/READER/
6b	Temperature, Upper Atmosphere	ERA5	https://www.ecmwf.int/en/forecasts/dataset/ecmwf-reanalysis-v5
6b	Wind, Upper Atmosphere	ERA5	https://www.ecmwf.int/en/forecasts/dataset/ecmwf-reanalysis-v5

Section 6c Ice-sheet surface mass balance

Sub-section	General Variable or Phenomenon	Specific dataset or variable	Source
6c	Ice-sheet surface mass balance	polar-oriented regional climate model (MAR)	https://arcticdata.io/catalog/view/doi%3A10.18739%2FA28G8FJ7F
6c	Ice-sheet surface mass balance	ERA5	https://www.ecmwf.int/en/forecasts/dataset/ecmwf-reanalysis-v5
6c	Ice-sheet surface mass balance	MERRA-2	http://gmao.gsfc.nasa.gov/reanalysis/MERRA-2/

Section 6d Ice-sheet melt extent and duration			
Sub-section	**General Variable or Phenomenon**	**Specific dataset or variable**	**Source**
6d	Ice-Sheet Surface Melt	DMSP-SSMIS	https://nsidc.org/data/nsidc-0001/versions/6
6d	Sea Ice Extent / Area / Concentration	Nimbus-7 SMMR Sea Ice Concentration	https://nsidc.org/data/nsidc-0007

Section 6e Ice-sheet mass balance			
Sub-section	**General Variable or Phenomenon**	**Specific dataset or variable**	**Source**
6e	Ice-Sheet Surface Height	ATLAS/ICESat-2 Land Height	https://nsidc.org/data/atl06/versions/5
6e	Ice-Sheet Surface Height	ICESat-2	https://icesat-2.gsfc.nasa.gov/
6e	Ice-Sheet Mass	GRACE - GRACE FO CRI	https://podaac.jpl.nasa.gov/dataset/TELLUS_GRAC-GRFO_MASCON_CRI_GRID_RL06_V2

Section 6f Sea-ice extent, concentration, and seasonality			
Sub-section	**General Variable or Phenomenon**	**Specific dataset or variable**	**Source**
6f	Sea Ice Duration	Near-Real-Time DMSP SSM/I-SSMIS Daily Polar Gridded	https://nsidc.org/data/nsidc-0081/versions/2
6f	Sea Ice Duration	Nimbus-7 SMMR and DMSP SSM/I (Bootstrap)	https://nsidc.org/data/nsidc-0079/versions/3
6f	Sea Surface Temperature	NOAA Optimum Interpolation SST (OISST) v2.1	https://www.ncei.noaa.gov/products/optimum-interpolation-sst

Section 6g Southern Ocean

Sub-section	General Variable or Phenomenon	Specific dataset or variable	Source
6g1	Sea Surface Temperature	NOAA Optimum Interpolation SST (OISST) v2.1	https://www.ncei.noaa.gov/products/optimum-interpolation-sst
6g1	Sea Surface Salinity	Argo monthly climatology	https://sio-argo.ucsd.edu/RG_Climatology.html
6g1	Mixed Layer Depth	Argo monthly climatology	https://sio-argo.ucsd.edu/RG_Climatology.html
6g2	Surface Heat flux	ERA5	https://www.ecmwf.int/en/forecasts/dataset/ecmwf-reanalysis-v5
6g3	Ocean Heat Content	Argo monthly climatology	https://sio-argo.ucsd.edu/RG_Climatology.html
6g4	Dissolved Oxygen	Argo profiling floats	https://argo.ucsd.edu/data/
6g4	Ocean Chlorophyll	ocean colour climate change initiative (OC-CCI) product v6.0	https://www.oceancolour.org/

Section 6h 2023 Antarctic ozone hole

Sub-section	General Variable or Phenomenon	Specific dataset or variable	Source
6h	Cloud Volume	CALIPSO	http://www-calipso.larc.nasa.gov
6h	Temperature, [Near] Surface	MERRA-2	http://gmao.gsfc.nasa.gov/reanalysis/MERRA-2/
6h	Temperature, upper atmosphere	MERRA-2	https://gmao.gsfc.nasa.gov/reanalysis/MERRA-2/
6h	Ozone, Total Column and Stratospheric	Aura MLS	http://disc.sci.gsfc.nasa.gov/Aura/data-holdings/MLS/index.shtml
6h	Ozone, Total Column and Stratospheric	Ozone Mapping Istrument (OMI) Ozone Mapping & Profiler Suite (OMPS), Total Ozone Mapping Spectrum (TOMS), Earth Probe TOMS (EPTOMS)	https://ozoneaq.gsfc.nasa.gov/data/ozone/
6h	Ozone, Lower Stratosphere	Ozonesonde	https://gml.noaa.gov/dv/spo_oz/

References

Adusumilli, S., H. A. Fricker, B. Medley, L. Padman, and M. R. Siegfried, 2020: Interannual variations in meltwater input to the Southern Ocean from Antarctic ice shelves. *Nat. Geosci.*, **13**, 616–620, https://doi.org/10.1038/s41561-020-0616-z.

—— , —— , and A. S. Gardner, 2023: Ice-sheet mass balance [in "State of the Climate in 2022"]. *Bull. Amer. Meteor. Soc.*, **104** (9), S341–S343, https://doi.org/10.1175/BAMS-D-23-0077.1.

Agosta, C., and Coauthors, 2019: Estimation of the Antarctic surface mass balance using the regional climate model MAR (1979–2015) and identification of dominant processes. *Cryosphere*, **13**, 281–296, https://doi.org/10.5194/tc-13-281-2019.

Arthur, J. F., C. R. Stokes, S. S. R. Jamieson, J. Rachel Carr, A. A. Leeson, and V. Verjans, 2022: Large interannual variability in supraglacial lakes around East Antarctica. *Nat. Commun.*, **13**, 1711, https://doi.org/10.1038/s41467-022-29385-3.

Baiman, R., A. C. Winters, J. Lenaerts, and C. A. Shields, 2023: Synoptic drivers of atmospheric river induced precipitation near Dronning Maud Land, Antarctica. *J. Geophys. Res. Atmos.*, **128**, e2022JD037859, https://doi.org/10.1029/2022JD037859.

Banwell, A. F., D. R. MacAyeal, and O. V. Sergienko, 2013: Breakup of the Larsen B Ice Shelf triggered by chain reaction drainage of supraglacial lakes. *Geophys. Res. Lett.*, **40**, 5872–5876, https://doi.org/10.1002/2013GL057694.

—— , N. Wever, D. Dunmire, and G. Picard, 2023: Quantifying Antarctic-wide ice-shelf surface melt volume using microwave and firn model data: 1980 to 2021. *Geophys. Res. Lett.*, **50**, e2023GL102744, https://doi.org/10.1029/2023GL102744.

Beadling, R. L., N. M. Freeman, G. A. MacGilchrist, M. Mazloff, J.-R. Shi, A. F. Thompson, and E. Wilson, 2022: Southern Ocean [in "State of the Climate in 2021"]. *Bull. Amer. Meteor. Soc.*, **103** (8), S329–S332, https://doi.org/10.1175/BAMS-D-22-0078.1.

Bell, R. E., A. F. Banwell, L. D. Trusel, and J. Kingslake, 2018: Antarctic surface hydrology and impacts on ice-sheet mass balance. *Nat. Climate Change*, **8**, 1044–1052, https://doi.org/10.1038/s41558-018-0326-3.

Blunden, J., T. Boyer, and E. Bartow-Gillies, Eds., 2023: "State of the Climate in 2022." Bull. *Amer. Meteor. Soc.*, **104** (9), S1–S501, https://doi.org/10.1175/2023BAMSStateoftheClimate.1.

Cai, W., and Coauthors, 2023: Southern Ocean warming and its climatic impacts. *Sci. Bull.*, **68**, 946–960, https://doi.org/10.1016/j.scib.2023.03.049.

Carr, J. L., Á. Horváth, D. L. Wu, and M. D. Friberg, 2022: Stereo plume height and motion retrievals for the record-setting Hunga Tonga-Hunga Ha'apai eruption of 15 January 2022. *Geophys. Res. Lett.*, **49**, e2022GL098131, https://doi.org/10.1029/2022GL098131.

Cavalieri, D. J., C. L. Parkinson, P. Gloersen, and H. J. Zwally, 1996: Sea ice concentrations from Nimbus-7 SMMR and DMSP SSM/I-SSMIS passive microwave data, version 1. NASA National Snow and Ice Data Center Distributed Active Archive Center, accessed 12 March 2024, https://doi.org/10.5067/8GQ8LZQVL0VL.

Cheng, L., and Coauthors, 2022: Past and future ocean warming. *Nat. Rev. Earth Environ.*, **3**, 776–794, https://doi.org/10.1038/s43017-022-00345-1.

—— , and Coauthors, 2024: New record ocean temperatures and related climate indicators in 2023. *Adv. Atmos. Sci.*, **41**, 1068–1082, https://doi.org/10.1007/s00376-024-3378-5.

Clem, K. R., and R. L. Fogt, 2013: Varying roles of ENSO and SAM on the Antarctic Peninsula climate in austral spring. *J. Geophys. Res. Atmos.*, **118**, 11 481–11 492, https://doi.org/10.1002/jgrd.50860.

—— , and M. N. Raphael, Eds., 2023: Antarctica and the Southern Ocean [in "State of the Climate in 2022"]. *Bull. Amer. Meteor. Soc.*, **104** (9), S322–S365, https://doi.org/10.1175/BAMS-D-23-0077.1.

—— , D. Bozkurt, D. Kennett, J. C. King, and J. Turner, 2022: Central tropical Pacific convection drives extreme high temperatures and surface melt on the Larsen C Ice Shelf, Antarctic Peninsula. *Nat. Commun.*, **13**, 3906, https://doi.org/10.1038/s41467-022-31119-4.

—— , S. Barreira, S. Colwell, R. L. Fogt, L. M. Keller, M. A. Lazzara, D. E. Mikolajczyk, and T. Norton, 2023: Atmospheric circulation and surface observations [in "State of the Climate in 2022"]. *Bull. Amer. Meteor. Soc.*, **104** (9), S329–S332, https://doi.org/10.1175/BAMS-D-23-0077.1.

Comiso, J. C., 2017: Bootstrap sea ice concentrations from Nimbus-7 SMMR and DMSP SSM/I-SSMIS, version 3. NASA National Snow and Ice Data Center Distributed Active Archive Center, accessed 12 March 2024, https://doi.org/10.5067/7Q8HCCWS4I0R.

Datta, R. T., R. Baiman, Z. Yin, J. D. Wille, D. Dunmire, M. L. Maclennan, L. D. Trusel, and D. Bozkurt, 2023: Ice-sheet surface mass balance [in "State of the Climate in 2022"]. *Bull. Amer. Meteor. Soc.*, **104** (9), S336–S339, https://doi.org/10.1175/BAMS-D-23-0077.1.

de Boyer Montégut, C., G. Madec, A. S. Fischer, A. Lazar, and D. Iudicone, 2004: Mixed layer depth over the global ocean: An examination of profile data and a profile-based climatology. *J. Geophys. Res.*, **109**, C12003, https://doi.org/10.1029/2004JC002378.

Depoorter, M. A., J. L. Bamber, J. A. Griggs, J. T. M. Lenaerts, S. R. M. Ligtenberg, M. R. van den Broeke, and G. Moholdt, 2013: Calving fluxes and basal melt rates of Antarctic ice shelves. *Nature*, **502**, 89–92, https://doi.org/10.1038/nature12567.

DiGirolamo, N. E., C. L. Parkinson, D. J. Cavalieri, P. Gloersen, and H. J. Zwally, 2022: Sea ice concentrations from Nimbus-7 SMMR and DMSP SSM/I-SSMIS passive microwave data. NASA National Snow and Ice Data Center Distributed Active Archive Center, accessed 5 February 2024, https://doi.org/10.5067/MPYG15WAA4WX.

Ding, Q., and E. J. Steig, 2013: Temperature change on the Antarctic Peninsula linked to the tropical Pacific. *J. Climate*, **26**, 7570–7585, https://doi.org/10.1175/JCLI-D-12-00729.1.

Fleming, E. L., P. A. Newman, Q. Liang, and L. D. Oman, 2024: Stratospheric temperature and ozone impacts of the Hunga Tonga-Hunga Ha'apai water vapor injection. *J. Geophys. Res. Atmos.*, **129**, e2023JD039298, https://doi.org/10.1029/2023JD039298.

Frölicher, T. L., J. L. Sarmiento, D. J. Paynter, J. P. Dunne, J. P. Krasting, and M. Winton, 2015: Dominance of the Southern Ocean in anthropogenic carbon and heat uptake in CMIP5 models. *J. Climate*, **28**, 862–886, https://doi.org/10.1175/JCLI-D-14-00117.1.

Gelaro, R., and Coauthors, 2017: The Modern-Era Retrospective Analysis for Research and Applications, version 2 (MERRA-2). *J. Climate*, **30**, 5419–5454, https://doi.org/10.1175/JCLI-D-16-0758.1.

Gerrish, L., L. Ireland, P. Fretwell, and P. Cooper, 2023: High resolution vector polygons of the Antarctic coastline, version 7.8. BAS Data Catalogue, accessed 5 February 2024, https://doi.org/10.5285/C7FE759D-E042-479A-9ECF-274255B4F0A1.

Gloersen, P., 2006: Nimbus-7 SMMR polar gridded radiances and sea ice concentrations, version 1. NASA National Snow and Ice Data Center Distributed Active Archive Center, accessed 1 December 2019, https://doi.org/10.5067/QOZIVYV3V9JP.

Gorodetskaya, I. V., and Coauthors, 2023: Record-high Antarctic Peninsula temperatures and surface melt in February 2022: A compound event with an intense atmospheric river. *npj Climate Atmos. Sci.*, **6**, 202, https://doi.org/10.1038/s41612-023-00529-6.

Gossart, A., S. Helsen, J. T. M. Lenaerts, S. V. Broucke, N. P. M. van Lipzig, and N. Souverijns, 2019: An evaluation of surface climatology in state-of-the-art reanalyses over the Antarctic Ice Sheet. *J. Climate*, **32**, 6899–6915, https://doi.org/10.1175/JCLI-D-19-0030.1.

Gudmundsson, G. H., F. S. Paolo, S. Adusumilli, and H. A. Fricker, 2019: Instantaneous Antarctic Ice Sheet mass loss driven by thinning ice shelves. *Geophys. Res. Lett.*, **46**, 13 903–13 909, https://doi.org/10.1029/2019GL085027.

Hanna, E., and Coauthors, 2024: Short- and long-term variability of the Antarctic and Greenland ice sheets. *Nat. Rev. Earth Environ.*, **5**, 193–210, https://doi.org/10.1038/s43017-023-00509-7.

Henley, S. F., and Coauthors, 2020: Changing biogeochemistry of the Southern Ocean and its ecosystem implications. *Front. Mar. Sci.*, **7**, 581, https://doi.org/10.3389/fmars.2020.00581.

Hersbach, H., and Coauthors, 2020: The ERA5 global reanalysis. *Quart. J. Roy. Meteor. Soc.*, **146**, 1999–2049, https://doi.org/10.1002/qj.3803.

Hobbs, W., and Coauthors, 2024: Observational evidence for a regime shift in summer Antarctic sea ice. *J. Climate*, **37**, 2263–2275, https://doi.org/10.1175/JCLI-D-23-0479.1.

Huang, B., C. Liu, V. Banzon, E. Freeman, G. Graham, B. Hankins, T. Smith, and H.-M. Zhang, 2021: Improvements of the Daily Optimum Interpolation Sea Surface Temperature (DOISST) version 2.1. *J. Climate*, **34**, 2923–2939, https://doi.org/10.1175/JCLI-D-20-0166.1.

Josey, S. A., J. P. Grist, J. V. Mecking, B. I. Moat, and E. Schulz, 2023: A clearer view of Southern Ocean air–sea interaction using surface heat flux asymmetry. *Philos. Trans. Roy. Soc.*, **A381**, 20220067, https://doi.org/10.1098/rsta.2022.0067.

Kittel, C., and Coauthors, 2021: Diverging future surface mass balance between the Antarctic ice shelves and grounded ice sheet. *Cryosphere*, **15**, 1215–1236, https://doi.org/10.5194/tc-15-1215-2021.

Kramarova, N. A., and Coauthors, 2023: 2022 Antarctic ozone hole [in "State of the Climate in 2022"]. *Bull. Amer. Meteor. Soc.*, **104** (9), S355–S359, https://doi.org/10.1175/BAMS-D-23-0077.1.

Kromer, J. D., and L. D. Trusel, 2023: Identifying the impacts of sea ice variability on the climate and surface mass balance of West Antarctica. *Geophys. Res. Lett.*, **50**, e2023GL104436, https://doi.org/10.1029/2023GL104436.

Lenaerts, J. T. M., B. Medley, M. R. Van Den Broeke, and B. Wouters, 2019: Observing and modeling ice sheet surface mass balance. *Rev. Geophys.*, **57**, 376–420, https://doi.org/10.1029/2018RG000622.

MacFerrin, M., T. Mote, H. Wang, L. Liu, L. Montgomery, and T. Scambos, 2021: Ice sheet seasonal melt extent and duration [in "State of the Climate in 2020"]. *Bull. Amer. Meteor. Soc.*, **102** (8), S331–S334, , https://doi.org/10.1175/BAMS-D-21-0081.1.

—— , —— , A. Banwell, and T. Scambos, 2022: Ice sheet seasonal melt extent and duration [in "State of the Climate in 2021"]. *Bull. Amer. Meteor. Soc.*, **103** (8), S321–S323, https://doi.org/10.1175/BAMS-D-22-0078.1

—— , —— , —— , and —— , 2023: Ice-sheet seasonal melt extent and duration [in "State of the Climate in 2022"]. *Bull. Amer. Meteor. Soc.*, **104** (9), S339–S341, https://doi.org/10.1175/BAMS-D-23-0077.1.

Maclennan, M. L., J. T. M. Lenaerts, C. Shields, and J. D. Wille, 2022: Contribution of atmospheric rivers to Antarctic precipitation. *Geophys. Res. Lett.*, **49**, e2022GL100585, https://doi.org/10.1029/2022GL100585.

—— , and Coauthors, 2023: Climatology and surface impacts of atmospheric rivers on West Antarctica. *Cryosphere*, **17**, 865–881, https://doi.org/10.5194/tc-17-865-2023.

Manney, G. L., and Coauthors, 2011: Unprecedented Arctic ozone loss in 2011. *Nature*, **478**, 469–475, https://doi.org/10.1038/nature10556.

—— , and Coauthors, 2023: Siege in the southern stratosphere: Hunga Tonga-Hunga Ha'apai water vapor excluded from the 2022 Antarctic polar vortex. *Geophys. Res. Lett.*, **50**, e2023GL103855, https://doi.org/10.1029/2023GL103855.

Marshall, G. J., 2003: Trends in the southern annular mode from observations and reanalyses. *J. Climate*, **16**, 4134–4143, https://doi.org/10.1175/1520-0442(2003)016<4134:TITSAM>2.0.CO;2.

Maslanik, J., and J. Stroeve, 1999: Near-real-time DMSP SSM/I-SSMIS daily polar gridded sea ice concentrations (updated daily). National Snow and Ice Data Center, accessed 12 March 2024, https://doi.org/10.5067/U8C09DWVX9LM.

Massom, R. A., S. E. Stammerjohn, W. Lefebvre, S. A. Harangozo, N. Adams, T. A. Scambos, M. J. Pook, and C. Fowler, 2008: West Antarctic Peninsula sea ice in 2005: Extreme ice compaction and ice edge retreat due to strong anomaly with respect to climate. *J. Geophys. Res.*, **113**, C02S20, https://doi.org/10.1029/2007JC004239.

—— , T. A. Scambos, L. G. Bennetts, P. Reid, V. A. Squire, and S. E. Stammerjohn, 2018: Antarctic ice shelf disintegration triggered by sea ice loss and ocean swell. *Nature*, **558**, 383–389, https://doi.org/10.1038/s41586-018-0212-1.

Matsuoka, K., and Coauthors, 2018: Quantarctica. https://doi.org/10.21334/NPOLAR.2018.8516E961.

Medley, B., and E. R. Thomas, 2019: Increased snowfall over the Antarctic Ice Sheet mitigated twentieth-century sea-level rise. *Nat. Climate Change*, **9**, 34–39, https://doi.org/10.1038/s41558-018-0356-x.

Meier, W. N., H. Wilcox, M. A. Hardman, and J. S. Stewart, 2019: DMSP SSM/I-SSMIS daily polar gridded brightness temperatures, version 5. Subset: 37 & 19 GHz, h-polarization, 25 km grid, October 1987–April 2020. NASA National Snow and Ice Data Center Distributed Active Archive Center, accessed 11 February 2021, https://doi.org/10.5067/QU2UYQ6T0B3P.

Miles, B. W. J., and R. G. Bingham, 2024: Progressive unanchoring of Antarctic ice shelves since 1973. *Nature*, **626**, 785–791, https://doi.org/10.1038/s41586-024-07049-0.

Millán, L., and Coauthors, 2022: The Hunga Tonga-Hunga Ha'apai hydration of the stratosphere. *Geophys. Res. Lett.*, **49**, e2022GL099381, https://doi.org/10.1029/2022GL099381.

Morlighem, M., and Coauthors, 2020: Deep glacial troughs and stabilizing ridges unveiled beneath the margins of the Antarctic Ice Sheet. *Nat. Geosci.*, **13**, 132–137, https://doi.org/10.1038/s41561-019-0510-8.

Mote, T. L., 2007: Greenland surface melt trends 1973–2007: Evidence of a large increase in 2007. *Geophys. Res. Lett.*, **34**, L22507, https://doi.org/10.1029/2007GL031976.

—— , 2014: MEaSUREs Greenland Surface Melt Daily 25km EASE-Grid 2.0, version 1. NASA National Snow and Ice Data Center Distributed Active Archive Center, https://doi.org/10.5067/MEASURES/CRYOSPHERE/nsidc-0533.001.

—— , and M. R. Anderson, 1995: Variations in snowpack melt on the Greenland ice sheet based on passive-microwave measurements. *J. Glaciol.*, **41**, 51–60, https://doi.org/10.3189/S0022143000017755.

Mottram, R., and Coauthors, 2021: What is the surface mass balance of Antarctica? An intercomparison of regional climate model estimates. *Cryosphere*, **15**, 3751–3784, https://doi.org/10.5194/tc-15-3751-2021.

Newman, P. A., S. R. Kawa, and E. R. Nash, 2004: On the size of the Antarctic ozone hole. *Geophys. Res. Lett.*, **31**, L21104, https://doi.org/10.1029/2004GL020596.

—— , J. S. Daniel, D. W. Waugh, and E. R. Nash, 2007: A new formulation of equivalent effective stratospheric chlorine (EESC). Atmos. *Chem. Phys.*, **7**, 4537–4552, https://doi.org/10.5194/acp-7-4537-2007.

Orsi, A. H., T. Whitworth, and W. D. Nowlin, 1995: On the meridional extent and fronts of the Antarctic Circumpolar Current. *Deep-Sea Res. I*, **42**, 641–673, https://doi.org/10.1016/0967-0637(95)00021-W.

Otosaka, I. N., and Coauthors, 2023: Mass balance of the Greenland and Antarctic ice sheets from 1992 to 2020. *Earth Syst. Sci. Data*, **15**, 1597–1616, https://doi.org/10.5194/essd-15-1597-2023.

Paolo, F. S., H. A. Fricker, and L. Padman, 2015: Volume loss from Antarctic ice shelves is accelerating. *Science*, **348**, 327–331, https://doi.org/10.1126/science.aaa0940.

Parkinson, C. L., and N. E. DiGirolamo, 2021: Sea ice extents continue to set new records: Arctic, Antarctic, and global results. *Remote Sens. Environ.*, **267**, 112753, https://doi.org/10.1016/j.rse.2021.112753.

Pezzi, L., and Coauthors, 2023: Southern Ocean [in "State of the Climate in 2022"]. *Bull. Amer. Meteor. Soc.*, **104** (9), S351–S355, https://doi.org/10.1175/BAMS-D-23-0077.1.

Pitts, M. C., L. R. Poole, and R. Gonzalez, 2018: Polar stratospheric cloud climatology based on CALIPSO spaceborne lidar measurements from 2006 to 2017. *Atmos. Chem. Phys.*, **18**, 10 881–10 913, https://doi.org/10.5194/acp-18-10881-2018.

Pohl, B., and Coauthors, 2021: Relationship between weather regimes and atmospheric rivers in East Antarctica. *J. Geophys. Res. Atmos.*, **126**, e2021JD035294, https://doi.org/10.1029/2021JD035294.

Purich, A., and E. W. Doddridge, 2023: Record low Antarctic sea ice coverage indicates a new sea ice state. *Commun. Earth Environ.*, **4**, 314, https://doi.org/10.1038/s43247-023-00961-9.

Raphael, M. N., and Coauthors, 2016: The Amundsen Sea low: Variability, change, and impact on Antarctic climate. *Bull. Amer. Meteor. Soc.*, **97**, 111–121, https://doi.org/10.1175/BAMS-D-14-00018.1.

Reid, P. A., and R. A. Massom, 2022: Change and variability in Antarctic coastal exposure, 1979–2020. *Nat. Commun.*, **13**, 1164, https://doi.org/10.1038/s41467-022-28676-z.

Reid, P., S. Stammerjohn, R. A. Massom, S. Barreira, T. Scambos, and J. L. Lieser, 2023: Sea-ice extent, concentration, and seasonality [in "State of the Climate in 2022"]. *Bull. Amer. Meteor. Soc.*, **104** (9), S344–S348, https://doi.org/10.1175/BAMS-D-23-0077.1.

Reynolds, R. W., N. A. Rayner, T. M. Smith, D. C. Stokes, and W. Wang, 2002: An improved in situ and satellite SST analysis for climate. *J. Climate*, **15**, 1609–1625, https://doi.org/10.1175/1520-0442(2002)015<1609:AIISAS>2.0.CO;2.

Rignot, E., S. Jacobs, J. Mouginot, and B. Scheuchl, 2013: Ice-shelf melting around Antarctica. *Science*, **341**, 266–270, https://doi.org/10.1126/science.1235798.

Roemmich, D., and J. Gilson, 2009: The 2004–2008 mean and annual cycle of temperature, salinity, and steric height in the global ocean from the Argo Program. *Prog. Oceanogr.*, **82**, 81–100, https://doi.org/10.1016/j.pocean.2009.03.004.

Santee, M. L., and Coauthors, 2024: The influence of stratospheric hydration from the Hunga eruption on chemical processing in the 2023 Antarctic vortex. ESS Open Archive, https://doi.org/10.22541/essoar.170542085.55151307/v1.

Sathyendranath, S., and Coauthors, 2019: An ocean-colour time series for use in climate studies: The experience of the Ocean-Colour Climate Change Initiative (OC-CCI). *Sensors*, **19**, 4285, https://doi.org/10.3390/s19194285.

Scambos, T. A., J. A. Bohlander, C. A. Shuman, and P. Skvarca, 2004: Glacier acceleration and thinning after ice shelf collapse in the Larsen B embayment, Antarctica. *Geophys. Res. Lett.*, **31**, L18402, https://doi.org/10.1029/2004GL020670.

—— , E. Berthier, T. Haran, C. A. Shuman, A. J. Cook, S. R. M. Ligtenberg, and J. Bohlander, 2014: Detailed ice loss pattern in the northern Antarctic Peninsula: Widespread decline driven by ice front retreats. *Cryosphere*, **8**, 2135–2145, https://doi.org/10.5194/tc-8-2135-2014.

Shepherd, A., and Coauthors, 2012: A reconciled estimate of ice-sheet mass balance. *Science*, **338**, 1183–1189, https://doi.org/10.1126/science.1228102.

Smith, B., and Coauthors, 2020: Pervasive ice sheet mass loss reflects competing ocean and atmosphere processes. *Science*, **368**, 1239–1242, https://doi.org/10.1126/science.aaz5845.

—— , S. Dickinson, B. J. Jelley, T. A. Neumann, D. Hancock, and K. Harbeck, 2022: ATLAS/ICESat-2 L3B slope-corrected land ice height time series, version 5. NASA National Snow and Ice Data Center Distributed Active Archive Center, accessed 12 February 2024, https://doi.org/10.5067/ATLAS/ATL11.005.

Stammerjohn, S. E., D. G. Martinson, R. C. Smith, X. Yuan, and D. Rind, 2008: Trends in Antarctic annual sea ice retreat and advance and their relation to El Niño–Southern Oscillation and Southern Annular Mode variability. *J. Geophys. Res.*, **113**, C03S90, https://doi.org/10.1029/2007JC004269.

Taha, G., R. Loughman, P. R. Colarco, T. Zhu, L. W. Thomason, and G. Jaross, 2022: Tracking the 2022 Hunga Tonga-Hunga Ha'apai aerosol cloud in the upper and middle stratosphere using space-based observations. *Geophys. Res. Lett.*, **49**, e2022GL100091, https://doi.org/10.1029/2022GL100091.

Teder, N. J., L. G. Bennetts, P. A. Reid, and R. A. Massom, 2022: Sea ice-free corridors for large swell to reach Antarctic ice shelves. *Environ. Res. Lett.*, **17**, 045026, https://doi.org/10.1088/1748-9326/ac5edd.

The Firn Symposium Team, 2024: Firn on ice sheets. *Nat. Rev. Earth Environ.*, **5**, 79–99, https://doi.org/10.1038/s43017-023-00507-9.

Thomalla, S. J., S.-A. Nicholson, T. J. Ryan-Keogh, and M. E. Smith, 2023: Widespread changes in Southern Ocean phytoplankton blooms linked to climate drivers. *Nat. Climate Change*, **13**, 975–984, https://doi.org/10.1038/s41558-023-01768-4.

Thompson, D. W. J., J. C. Furtado, and T. G. Shepherd, 2006: On the tropospheric response to anomalous stratospheric wave drag and radiative heating. *J. Atmos. Sci.*, **63**, 2616–2629, https://doi.org/10.1175/JAS3771.1.

Trusel, L. D., Z. Pan, and M. Moussavi, 2022: Repeated tidally induced hydrofracture of a supraglacial lake at the Amery Ice Shelf grounding zone. *Geophys. Res. Lett.*, **49**, e2021GL095661, https://doi.org/10.1029/2021GL095661.

Turner, J., and Coauthors, 2019: The dominant role of extreme precipitation events in Antarctic snowfall variability. *Geophys. Res. Lett.*, **46**, 3502–3511, https://doi.org/10.1029/2018GL081517.

Van Wessem, J. M., and Coauthors, 2018: Modelling the climate and surface mass balance of polar ice sheets using RACMO2 – Part 2: Antarctica (1979–2016). *Cryosphere*, **12**, 1479–1498, https://doi.org/10.5194/tc-12-1479-2018.

Wang, Y., D. Zhou, A. Bunde, and S. Havlin, 2016: Testing reanalysis data sets in Antarctica: Trends, persistence properties, and trend significance. *J. Geophys. Res. Atmos.*, **121**, 12 839–12 855, https://doi.org/10.1002/2016JD024864.

Wiese, D. N., D.-N. Yuan, C. Boening, F. W. Landerer, and M. M. Watkins, 2023a: JPL GRACE Mascon Ocean, ice, and hydrology equivalent water height RL06.1 CRI filtered version 03. Ver. RL06.1Mv03. PO.DAAC, accessed 10 February 2023, https://doi.org/10.5067/TEMSC-3JC63.

——, ——, ——, ——, and ——, 2023b: Tellus level-4 ocean mass anomaly time series from JPL GRACE/GRACE-FO Mascon CRI filtered release 06.1 version 03. Ver. RL06.1Mv03. PO.DAAC, accessed 10 February 2023, https://doi.org/10.5067/TEMSC-AT613.

Wille, J. D., and Coauthors, 2021: Antarctic atmospheric river climatology and precipitation impacts. *J. Geophys. Res. Atmos.*, **126**, e2020JD033788, https://doi.org/10.1029/2020JD033788.

Wong, A. P. S., and Coauthors, 2020: Argo Data 1999–2019: Two million temperature-salinity profiles and subsurface velocity observations from a global array of profiling floats. *Front. Mar. Sci.*, **7**, 700, https://doi.org/10.3389/fmars.2020.00700.

WMO, 2022: Scientific Assessment of Ozone Depletion: 2022. GAW Rep. 278, 509 pp., https://csl.noaa.gov/assessments/ozone/2022/